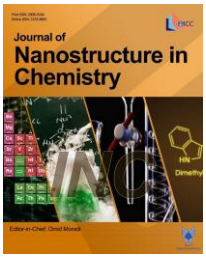

J. Nanostruct Chem. 2026; 16(3): 284-303

Journal of Nanostructure in Chemistry (JNSC)

https://doi.org/10.57647/jnsc.2026.1603.14

Research Article

Viscoelastic Janus Nanohydrogels for IL-1β Binding: Synthesis, Structure, and Release Kinetics

Lingyan Peng[1], Guohong Yuan[2], Guanghao Wu[3], Xiaohui Yin[4] , Yong Zhang[4], Xiangying Ouyang[1] , Jing Qiao[4,*]

[1]*Department of Periodontology, Peking University School and Hospital of Stomatology & National Center for Stomatology & National Clinical Research Center for Oral Diseases & National Engineering Research Center of Oral Biomaterials and Digital Medical Devices, Beijing, 100081, China*

[2]*National Research Institute for Family Planning National Human Genetic Resources Center*

[3]*School of Medical Technology, Beijing Institute of Technology, Beijing, 100081, China*

[4]*First Clinical Division, Peking University School and Hospital of Stomatology & National Center for Stomatology & National Clinical Research Center for Oral Diseases & National Engineering Research Center of Oral Biomaterials and Digital Medical Devices, Beijing, 100034, China*

[*] **Corresponding authors:** donaldshushu@aliyun.com; qiaojing@pkuss.bjmu.edu.cn

Article History:

Received:
25 December 2025

Revised:
27 January 2026

Accepted:
14 February 2026

Published in Issue:
30 June 2026

Abstract

Interleukin-1β (IL-1β) is a potent pro-inflammatory cytokine central to the pathogenesis of numerous autoinflammatory and chronic inflammatory diseases. Current systemic anti-IL-1β therapies, while effective, are associated with significant side effects, necessitating the development of materials for localized immunomodulation. This study reports the design, synthesis, and comprehensive characterization of a novel, dual-function Viscoelastic Janus Nanohydrogel (VJNH) platform for the simultaneous sequestration of IL-1β and controlled release of an anti-inflammatory therapeutic. VJNHs were synthesized with an asymmetric Au@SiO_2 inorganic core; the gold (Au) face was functionalized with a high-affinity DNA aptamer for IL-1β capture, while the silica (SiO_2) face served as an anchor for a viscoelastic hydrogel shell. This shell was formed via dynamic Schiff base (C=N) chemistry between aldehyde-functionalized hyaluronic acid (oHA) and amine-rich gelatin. Transmission electron microscopy (TEM) and X-ray photoelectron spectroscopy (XPS) confirmed the asymmetric Janus morphology and spatially segregated surface chemistry. Rheological analysis demonstrated the ECM-mimetic viscoelastic properties of the network, including high solid-like character ($G' > G''$) and rapid stress relaxation (relaxation time $\tau \approx 120$ s), attributed to the dynamic covalent linkages. A comparative study identified an optimal VJNH-2 (1:1 oHA:Gelatin) formulation, which exhibited superior IL-1β binding capacity (≈ 180 ng/mg). Surface plasmon resonance (SPR) analysis revealed high-affinity and specific binding, with an equilibrium dissociation constant (K_n) of 1.24 nM. Concurrently, the VJNHs demonstrated sustained, pH-responsive release of a model drug (Dexamethasone), fitting a Fickian diffusion mechanism (Higuchi and Korsmeyer-Peppas models). All VJNH formulations were non-cytotoxic to L929 fibroblasts. These results establish VJNHs as a sophisticated "sense-and-respond" platform, synergizing spatial, mechanical, and chemical functionalities for advanced, localized treatment of inflammatory disorders.

Keywords: Aptamer; Dexamethasone; Immunomodulation; Periodontitis; Schiff Base

Cite this article: Lingyan P., Guohong Y., Guanghao W., Xiaohui Y., Yong Zh., Xiangying O., Jing Q.Viscoelastic Janus Nanohydrogels for IL-1β Binding: Synthesis, Structure, and Release Kinetics. *J Nanostruct Chem* **16**, 284-303 (2026). https://doi.org/10.57647/jnsc.2026.1603.14

1. Introduction

The interleukin-1 (IL-1) family of cytokines comprises fundamental mediators of innate immunity and inflammatory responses [1]. Among these, IL-1β stands as the most extensively characterized and potent pro-inflammatory factor [2]. The biological activity of IL-1β is tightly regulated, requiring proteolytic processing of its inactive precursor, pro-IL-1β, into its mature form. This activation is typically mediated by the caspase-1 enzyme, which is activated by multi-protein complexes known as inflammasomes [3]. Once secreted, mature IL-1β binds to its cognate receptor, IL-1R1, initiating a potent downstream signaling cascade via TRAF6 and the IKK complex, ultimately leading to the activation of the transcription factor NF-κB, a master regulator of inflammatory gene expression [4]. In the context of oral diseases, IL-1β is recognized as a master cytokine driving the progression of periodontitis. Elevated IL-1β levels in gingival crevicular fluid and periodontal tissues correlate strongly with tissue destruction, alveolar bone resorption, and clinical attachment loss. The cytokine stimulates osteoclast differentiation through RANKL signaling, amplifies local neutrophil infiltration, and sustains chronic inflammation in periodontal pockets. Therefore, localized control of IL-1β activity within periodontal microenvironments is considered a critical therapeutic objective.

The dysregulated or exaggerated production of IL-1β is not merely a symptom but a causal driver in a wide spectrum of human pathologies. This includes rare monogenic autoinflammatory conditions, such as cryopyrin-associated periodic syndromes (CAPS), which are often caused by gain-of-function mutations in inflammasome-related genes leading to constitutive IL-1β secretion. Beyond these severe, rare conditions like DIRA (deficiency of the IL-1 receptor antagonist) [5], IL-1β has been validated as a critical therapeutic target in highly prevalent, chronic inflammatory and degenerative diseases, including rheumatoid arthritis (RA) [3], gout and acute gouty arthritis, inflammatory bowel disease (IBD) [6], and type 2 diabetes [3]. Furthermore, IL-1β plays a key role in both the induction and maintenance of chronic pain states by mediating glia-neuron interactions [7].

The unequivocal success of IL-1β-neutralizing biologics has confirmed its pivotal role in these diseases. Current therapeutics include anakinra, a recombinant IL-1 receptor antagonist; rilonacept, a soluble decoy receptor or "IL-1 Trap" [8]; and canakinumab, a human monoclonal antibody that specifically neutralizes IL-1β. While clinically effective, these therapies are administered systemically, resulting in global neutralization of IL-1β. This systemic action, however, is their primary drawback, as it can compromise the host's innate immune response and increase the risk of infections. This limitation highlights a significant unmet clinical need for novel therapeutic strategies that can provide potent and localized immunomodulation at the specific site of inflammation, such as inflamed periodontal tissues or arthritic joints, without inducing systemic immunosuppression.

We hypothesize that a localized "cytokine sink," or an immuno-isolating matrix capable of active sequestration, represents a superior therapeutic paradigm [9]. In chronic periodontitis, where IL-1β is persistently overexpressed in gingival tissues, creating a local “cytokine sink” capable of capturing excess cytokines and releasing anti-inflammatory agents could suppress destructive immune responses while preserving normal healing. Nanohydrogels are exemplary candidates for this role. Their highly hydrated, three-dimensional porous networks mimic the natural extracellular matrix, exhibit excellent biocompatibility, and can be engineered to capture and neutralize inflammatory cytokines [10]. This strategy shifts the therapeutic focus from systemic neutralization to localized sequestration, thereby terminating the inflammatory cascade at its source [11]. To achieve specific, high-affinity capture, these hydrogels can be functionalized with synthetic DNA or RNA aptamers. Aptamers function as "chemical antibodies," offering specific target recognition with advantages over proteins, such as higher thermal stability, lower immunogenicity, and greater synthetic flexibility [12].

However, traditional nanohydrogels are isotropic materials, with properties averaged over their volume, which limits functional complexity. We propose a "Janus" architecture, named for the two-faced Roman god [13], to overcome this limitation. Janus particles (JPs) are inherently asymmetric, possessing two distinct faces with different chemical or physical properties. This asymmetric design is a powerful concept in bioengineering, enabling the spatial segregation of distinct or even incompatible modalities, such as diagnostics and therapeutics (theranostics) [14], or the integration of adhesive and anti-adhesive surfaces on a single construct [15]. In our proposed design, one face of the nanoparticle will be dedicated to high-affinity IL-1β aptamer binding, while the other face will serve as the anchor for a therapeutic hydrogel.

Furthermore, most synthetic hydrogels are crosslinked with permanent covalent bonds, resulting in purely elastic materials. This is a poor mechanical match for native biological tissues, which are inherently viscoelastic; they dynamically absorb, store, and dissipate mechanical energy [16]. Importantly, viscoelasticity also provides engineering advantages for localized immunomodulation: stress relaxation and network rearrangement can enable conformal adaptation to irregular defects, maintain intimate interfacial contact under cyclic mechanical perturbations, and improve the structural resilience of a

10.57647/jnsc.2026.1603.14

local “cytokine sink” after deformation or minor damage, thereby supporting sustained sequestration performance.

These concepts are consistent with the broader mechanobiology literature demonstrating that stress-relaxing hydrogels modulate cell spreading, matrix remodeling, and in vivo scaffold remodeling outcomes (often independent of initial modulus), highlighting viscoelasticity as a functional design axis rather than a purely biomimetic descriptor [17]. In our system, the dynamic Schiff-base network yields measurable stress relaxation (τ on the order of minutes) and self-healing, while maintaining solid-like character ($G' > G''$), properties expected to facilitate retention and mechanical compatibility at inflamed sites while preserving transport pathways needed for IL-1β access to aptamer binding domains and for controlled drug diffusionThis viscoelastic property is crucial for regulating cellular behavior and for physical integration with dynamic tissues [18]. We will achieve this biomimicry by fabricating our nanohydrogel shell using dynamic covalent chemistry (DCC) [19]. Specifically, we will utilize the reversible Schiff base (imine) linkage [20] formed between aldehyde-functionalized hyaluronic acid (oHA) and the primary amines of gelatin [21]. This dynamic network is expected to be injectable, self-healing [22], and capable of stress relaxation, thereby mimicking the mechanical microenvironment of the extracellular matrix (ECM) [16]. Because Schiff-base (imine) linkages are reversible, the same bond exchange that enables stressnce hydrolytic stability during prolonged exposure to physiological fluids. Therefore, beyond short-time rheological characterization, it is important to evaluate whether the integrated nanocomposite (aptamer–Au face, silica cap, and oHA–gelatin shell) maintains colloidal integrity and IL-1β sequestration performance after aging in buffered and protein-containing media at 37 °C, where protein adsorption can alter apparent size and surface charge and silica frameworks can gradually dissolve.

An additional, clinically relevant design axis for localized delivery is responsiveness to microenvironmental cues. Among these, pH is a simple but informative varssue spaces are typically near pH 7.3–7.4, whereas inflammatory and diseased microenvironments can deviate from this range, reflecting altered metabolism, perfusion, and immune activity. In the oral cavity, direct microelectrode measurements have reported gingival crevice/periodontal pocket pH values that are often close to neutral on average (≈6.9), yet local heterogeneity can occur within biofilm-rich lesions. Because the oHA–gelatin shell is built from ionizable groups and dynamic Schiff-base linkages whose network state couples to proton activity, pH-dependent swelling provides a mechanistic route to tune mesh size and therefore diffusion of encapsulated small-molecule therapeutics. We therefore evaluated release at pH 7.4 and under an acidic challenge (pH 5.5) to quantify how this cue alters swelling and drug transport in our system [23]. This work reports the rational design, synthesis, and exhaustive characterization of a novel Viscoelastic Janus Nanohydrogel (VJNH) platform. We aim to: (1) confirm the Janus morphology and asyionalization using high-resolution electron microscopy and surface-sensitive spectroscopy; (2) quantify the viscoelastic and self-healing properties derived from the dynamic Schiff base chemistry using rheological analysis; (3) conduct a comparative study of different VJNH formulations to optimize their physicochemical properties; and (4) demonstrate the platform’s dual functionality by quantifying its high-affinity binding kinetics for IL-1β (via ELISA and SPR) and its sustained release kinetics of a model anti-inflammatory drug, with an emphasis on how local pH—an established microenvironmental variable in inflamed tissues—modulates hydrogel swelling/mesh size and thereby diffusion-controlled release.

2. Materials and Methods

2.1. Materials

Gold(III) chloride trihydrate ($HAuCl_4 \cdot 3H_2O$), trisodium citrate dihydrate (99.0%), tetraethyl orthosilicate (TEOS, 99.9%), (3-Aminopropyl)triethoxysilane (APTES, 99%), glutaraldehyde (Grade I, 50% in H_2O), hyaluronic acid sodium salt (HA, 50 kDa), gelatin (from porcine skin, Type A, 300 bloom), sodium periodate ($NaIO_4$), 3-methyl-2-benzothiazolinone hydrazone (MBTH), Dexamethasone (DEX), N-hydroxysuccinimide (NHS), N-(3-Dimethylaminopropyl)-N′-ethylcarbodiimide hydrochloride (EDC), and all analytical-grade solvents were purchased from Sigma-Aldrich. Cetyltrimethylammonium bromide (CTAB) and hexadecane (99%) were obtained from Fluka. The thiolated human IL-1β DNA aptamer (5'-SH-$(CH_2)_6$-GCA TCT GGT CAT GCT ACC TGA GTC GAT GCT GCA GCT-3') and a non-specific thiolated control oligo (5'-SH- $(CH_2)_6$-T_{30}-3') were custom-synthesized by IDT DNA Technologies [24]. Recombinant human IL-1β, human TNF-α, and bovine serum albumin (BSA) were purchased from R&D Systems. Human IL-1β Quantikine ELISA kits were also sourced from R&D Systems. L929 mouse fibroblast cells were obtained from the American Type Culture Collection (ATCC).

2.2. Synthesis of Au@SiO_2 Janus Nanoparticle Cores

Gold nanopartidiameter of 50 nm were first synthesized via the classic Turkevich citrate reduction method. Subsequently, the Au@SiO_2 Janus nanoparticles were fabricated using a modified interfacial Pickering emulsion method. Briefly, 10 mL of the aqueous AuNP suspension

10.57647/jnsc.2026.1603.14

was added to 20 mL of hexadecane containing 50 mg of CTAB [25]. The mixture was sonicated for 30 minutes to form a stable oil-in-water Pickering emulsion, which forces the AuNPs to the oil–water interface. The spatially selective growth of silica arises from this interfacial confinement: TEOS hydrolysis and the generation of reactive silanol/oligosilicate species are promoted in the aqueous, base-catalyzed domain, so condensation occurs preferentially on the AuNP hemisphere exposed to water, whereas the oil-immersed hemisphere is water-depleted and diffusion-limited for hydrolyzed silicate oligomers, suppressing nucleation and yielding an asymmetric cap. This interface-directed sol–gel mechanism has been widely used for site-selective silica growth and Janus silica architectures on noble-metal nanoparticles. To this emulsion, 500 µL of TEOS was added, followed by 200 µL of 25% v/v ammonium hydroxide to catalyze polycondensation. The reaction proceeded for 12 hours under gentle stirring, forming an Au@SiO_2 'acorn-like' Janus core. The resulting Au@SiO_2 Janus particles were collected by breaking the emulsion with ethanol, followed by five cycles of centrifugation and washing with ethanol and water. The particles were then calcined at 450 °C for 4 hours to remove CTAB and other organic residues. Because CTAB acts as a structure-directing template during silica formation, its removal generates mesoporous silica, consistent with established surfactant-templated mesoporous silica chemistry.

2.3. Asymmetric Surface Functionalization

The Janus cores were dually functionalized in a sequential manner. First, the Au face was functionalized with the thiolated IL-1β aptamer. The Au@SiO_2 particles were suspended in a 10 mM phosphate buffer (pH 7.4). The thiolated aptamer was added to a final concentration of 2 µM and allowed to react for 24 hours at room temperature to form stable Au-S bonds [26]. Subsequently, 1-mercapto-6-hexanol (MCH) was added to a final concentration of 1 mM and incubated for 2 hours to passivate any remaining bare gold surface and promote an upright orientation of the aptamer.

Second, the silica face was modified to provide an anchoring point for the hydrogel shell. The aptamer-functionalized particles were washed and resuspended in dry toluene. APTES (1% v/v) was added, and the mixture was refluxed for 6 hours to functionalize the silica surface with primary amines. After washing, the particles were resuspended in PBS (pH 7.0), and glutaraldehyde (2.5% v/v) was added.

The reaction proceeded for 2 hours. This step reacts one aldehyde group of glutaraldehyde with the amines on the silica surface, leaving the second aldehyde group exposed and available to react with the hydrogel precursors.

2.4. Synthesis of Viscoelastic Janus Nanohydrogels (VJNHs)

The viscoelastic shell was formed from oxidized hyaluronic acid (oHA) and gelatin via Schiff base chemistry. HA was first oxidized to oHA by reacting 1.0 g of HA with 0.5 g of $NaIO_4$ in 100 mL of water for 6 hours in the dark [27]. The reaction was quenched with ethylene glycol, and the oHA was purified by dialysis and lyophilization. The degree of oxidation (percentage of diol units converted to dialdehydes) was determined to be ≈ 50% using an MBTH assay [27].

To form the nanohydrogels, a nanoemulsion method was employed. Three different formulations were prepared by varying the oHA:Gelatin weight ratio: VJNH-1 (1:2), VJNH-2 (1:1), and VJNH-3 (2:1). For VJNH-2, 10 mg of the dually-functionalized Au@SiO_2 cores were suspended in 1 mL of a 1% w/v gelatin solution in PBS (pH 7.4). This suspension was added dropwise to 1 mL of a 1% w/v oHA solution in PBS (pH 7.4) under high-power sonication in an ice bath. The dynamic Schiff base (C=N) reaction occurred *in situ*, crosslinking the gelatin (amines) and oHA (aldehydes) to form the shell, which simultaneously grafted onto the aldehyde-functionalized silica surface. The resulting VJNHs were stirred for 4 hours to mature. The final nanohydrogels were then purified by repeated centrifugal washing to remove unreacted oHA/gelatin, soluble Schiff-base byproducts, and any trace amphiphiles that could be carried over from the Janus core preparation. Specifically, the reaction dispersion was centrifuged at 12,000 × g for 15 min at 4 °C to pellet the VJNHs, the supernatant containing soluble/unreacted species was discarded, and the pellet was gently resuspended in phosphate-buffered saline (PBS, pH 7.4). This centrifugation–resuspension washing cycle was repeated three times using PBS as the washing medium. To further minimize any potential residual emulsifier contamination, an additional wash was performed using 95% ethanol followed by a final PBS wash, after which the purified VJNHs were resuspended in PBS (pH 7.4) for subsequent experiments. For drug release studies, DEX was incorporated at 10% w/w relative to the total polymer content by dissolving it in the gelatin solution prior to emulsification. This loading was selected after preliminary formulation optimization across a 5–20% w/w range, using qualitative and performance-based criteria aligned with the current study objectives: stable nanoemulsification without visible DEX aggregation/crystallization, preservation of hydrogel network integrity/handling during synthesis, and sustained release without evidence of pronounced early dose dumping. We emphasize that 10% w/w is a deliberately selected working loading for the present platform/mechanism study rather than a definitive universal optimum; systematic loading-dependent

10.57647/jnsc.2026.1603.14

comparisons of release and anti-inflammatory outcomes are outlined as future work. The need to tune corticosteroid loading to balance sustained exposure and minimize burst-related safety concerns is well documented in polymeric delivery systems.

2.5. Synthesis of Control Samples

Two control samples were prepared. A Homogeneous Nanohydrogel (HNH) was synthesized using the same procedure as VJNH-2 (1:1 oHA:Gelatin) but without the addition of the Au@SiO_2 Janus cores [28]. A Blank Janus (VJNH-Blank) particle was prepared identically to VJNH-2, but the non-specific thiolated control oligo was used in place of the IL-1β aptamer.

2.6. Performance and Kinetic Assays

Rheological properties of bulk hydrogels (prepared at 5% w/v total polymer with the same oHA:Gel ratios) were analyzed on a TA Instruments AR-G2 rotational rheometer with a 20 mm parallel plate geometry. Oscillatory frequency sweeps (0.1–100 rad/s, 1% strain) and stress-relaxation tests (1% constant strain) were performed at 37 °C.

Swelling studies were conducted by immersing 10 mg of lyophilized VJNHs (W_d) in PBS (pH 7.4 or 5.5) at 37 °C. At predetermined time points, swollen samples were collected by centrifugation, blotted to remove excess surface water, and weighed (W_s). The Equilibrium Swelling Ratio (ESR) was calculated as ESR = [(W_s - W_d) / W_d] × 100% [29].

In vitro cytotoxicity was evaluated using an extract-based MTT assay on L929 fibroblasts [30]. VJNH extracts were prepared by incubating stein complete culture medium (DMEM containing 10% FBS and 1% penicillin/streptomycin) at 37 °C for 24 h at a material loading of 1.0 mg/mL, following the general elution (extract) approach recommended for cytotoxicity evaluation (ISO 10993-5/10993-12). The resulting eluates were clarified by centrifugation to remove any residual hydrogel debris and then sterile-filtered (0.22 μm) before being applied to cells; this ensured that cells were exposed to soluble/leachable components rather than to suspended particles. L929 cells were seeded in 96-well plates at 1.0 × 10^4 cells/well (100 μL per well) and allowed to attach for 24 h. VJNH extracts (0.1–1.0 mg/mL in complete culture medium) were then added and incubated for 24, 48, and 72 h. At each time point, the medium was replaced with fresh medium containing MTT (0.5 mg/mL) and incubated for 3–4 h at 37 °C, after which the supernatant was carefully removed and the resulting formazan crystals were dissolved in DMSO (100 μL/well) with gentle shaking for 10 min. Absorbance was read at 570 nm (with background correction using a reference wavelength when available) and normalized to untreated cells. To exclude nanomaterial-related optical/chemical interference, a material-only control was established in parallel by incubating each VJNH extract concentration with MTT under identical conditions in cell-free wells; the corresponding background absorbance was subtracted from sample readings to ensure OD changes reflect cellular metabolic activity rather than direct interactions between VJNH components and the tetrazolium/formazan system [31].

IL-1β sequestration kinetics were measured by a depletion assay. VJNH samples (1 mg/mL) were incubated in a 500 pg/mL solution of IL-1β in PBS with 0.1% BSA at 37 °C. The supernatant was sampled at time points (0–24h), and the concentration of free, unbound IL-1β was quantified using a commercial sandwich ELISA kit. Binding specificity was tested by incubating VJNH-2 in a "cocktail" solution containing 500 pg/mL each of IL-1β, TNF-α, and BSA.

IL-1β binding kinetics were quantified using a Biacore T200 Surface Plasmon Resonance (SPR) instrument. VJNH-2 (hydrodynamic diameter ≈ 245.8 nm; PDI ≈ 0.15, measured by DLS) was immobilized on a CM5 sensor chip by direct covalent amine coupling. Briefly, the carboxymethyl-dextran surface was activated using standard EDC/NHS chemistry, and VJNH-2 was introduced under conditions favoring electrostatic preconcentration, followed by formation of covalent linkages between surface-activated esters on the CM5 matrix and accessible primary amines within the gelatin-rich shell of VJNH-2; remaining reactive esters were blocked with ethanolamine. This direct immobilization strategy yields a stable surface over multi-cycle injections and avoids reliance on a reversible ‘capture’ layer. To minimize risks associated with particulate ligands (e.g., aggregation-related transport artifacts), VJNH-2 dispersions were prepared immediately before analysis and handled under conditions that maintain colloidal stability as supported by the low PDI reported in Table 1. Recombinant IL-1β (analyte) was injected at multiple concentrations (0–20 nM). Sensorgrams were processed by reference channel subtraction and blank (buffer) subtraction prior to kinetic fitting to reduce contributions from bulk refractive index changes and non-specific effects, consistent with standard SPR data treatment; solvent correction was not applied because the analyte solutions did not contain organic cosolvents (e.g., DMSO). Processed data were globally fitted to a 1:1 Langmuir binding model to obtain kon, koff, and K_d [32]. In vitro drug release kinetics were studied using DEX-loaded VJNHs. Samples (10 mg) were placed in a dialysis cassette (10 kDa MWCO) and immersed in 50 mL of release buffer (PBS at pH 7.4 or 5.5) at 37 °C with stirring. Aliquots (1 mL) were withdrawn at time points and replaced with fresh buffer. The concentration of released

DEX was quantified by UV-vis absorbance at 242 nm. Cumulative release data were fitted to zero-order, first-order, Higuchi, and Korsmeyer-Peppas [33] kinetic models to elucidate the release mechanism [34].

2.7. Physiological Stability of VJNHs

To evaluate long-term physiological stability, VJNH-2 dispersions (1 mg mL^{-1}) were incubated at 37 °C in (i) PBS (pH 7.4) and (ii) cell culture mediine serum (FBS). At predetermined time points (1, 7, 14, and 28 days), samples were collected and characterized for hydrodynamic diameter, PDI, and ζ-potential by DLS. Structural integrity was assessed by TEM after 28 days and by FTIR to monitor retention of the imine-associated band contribution (~1655 cm^{-1}). Functional stability was assessed by measuring residual IL-1β binding capacity using the ELISA depletion protocol (500 pg mL^{-1} IL-1β, 37 °C), comparing aged versus freshly prepared VJNH-2. This protocol follows common approaches used to quantify time-dependent stability of Schiff-base hydrogels and nanoparticle behavior in protein-containing media.

3. Results and Discussion

3.1. Synthesis and Physicochemical Characterization

The multistep synthesis of the Viscoelastic Janus Nanohydrogels (VJNHs) is depicted in Fig. 1. The strategy was designed to create a multifunctional nanostructure by converging two distinct fabrication paradigms: (1) an interfacial sol-gel reaction on a Pickering emulsion template to produce the asymmetric Au@SiO_2 inorganic core, and (2) *in situ* dynamic covalent crosslinking of biopolymers to form the viscoelastic shell [35].

The sequential chemical modifications were confirmed by spectroscopic analyses, as shown in Fig. 2. The FTIR spectrum (Fig. 2A) of native HA displayed characteristic peaks for O-H stretching (3400 cm^{-1}), C=O stretching of the carboxylate (≈ 1610 cm^{-1}), and C-O-C stretching (≈ 1045 cm^{-1}) Upon oxidation with $NaIO_4$, the spectrum of oHA showed a new, distinct shoulder at ≈ 1730 cm^{-1}, which is attributed to the C=O stretching vibration of the newly formed aldehyde groups.[41, 51] The spectrum of gelatin (Type A) showed prominent Amide I (≈ 1650 cm^{-1}) and Amide II (≈ 1540 cm^{-1}) bands. In the final VJNH-2 spectrum, the aldehyde shoulder at 1730 cm^{-1} was significantly diminished, and a new peak emerged at ≈ 1655 cm^{-1}. This peak is a composite of the gelatin Amide I band and the newly formed C=N imine (Schiff base) linkage [36], confirming the successful dynamic crosslinking reaction between the oHA aldehydes and gelatin amines.[41] UV-vis spectroscopy (Fig. 2B) was used to monitor the plasmonic core and aptamer conjugation. The initial 50 nm AuNPs exhibited a sharp surface plasmon resonance (SPR) peak at 530 nm. After silica capping (Au@SiO_2), this peak red-shifted to ≈ 545 nm due to the change in the local dielectric environment. A further red-shift to 552 nm was observed for the final VJNH-2, consistent with the formation of the dense hydrogel shell. Critically, the VJNH-2 spectrum also displayed a strong absorbance peak at 260 nm, confirming the successful conjugation of the DNA aptamer onto the gold surface [30].

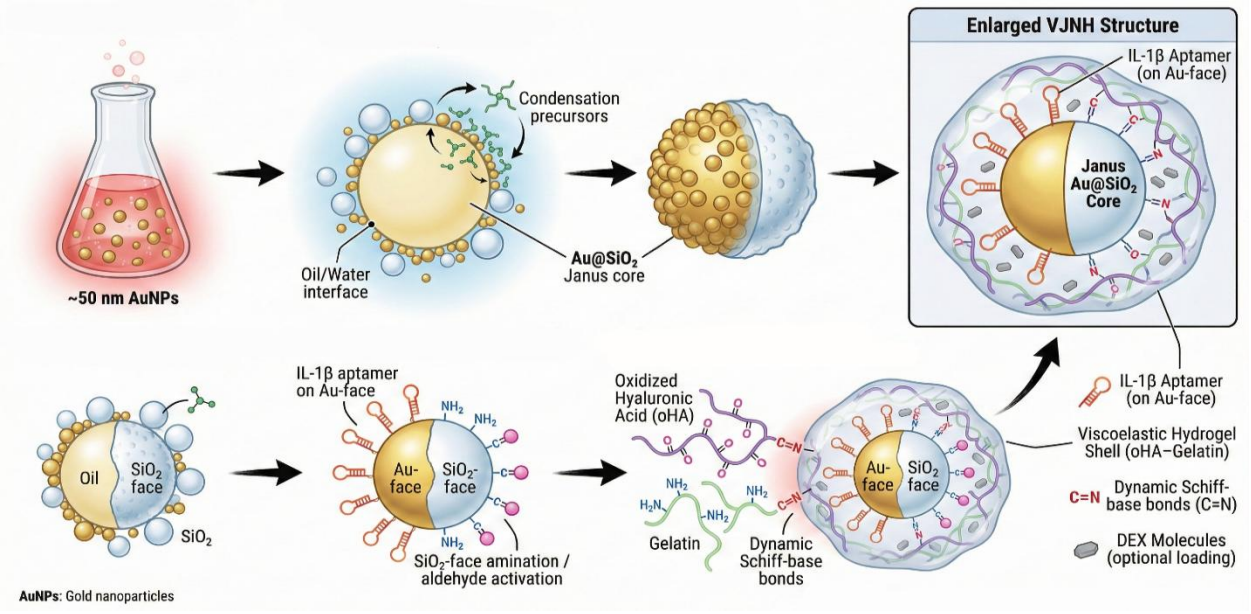

Figure 1. Schematic illustration of the Viscoelastic Janus Nanohydrogel (VJNH) design and fabrication: (i) 50 nm AuNP synthesis; (ii) interfacial TEOS sol–gel on a Pickering emulsion to form Au@SiO_2 Janus cores; (iii) selective Au-face IL-1β aptamer conjugation and SiO_2-face amination/aldehyde activation; (iv) in situ dynamic Schiff-base crosslinking between oxidized hyaluronic acid (oHA) and gelatin to yield a viscoelastic shell; optional DEX loading in the shell

10.57647/jnsc.2026.1603.14

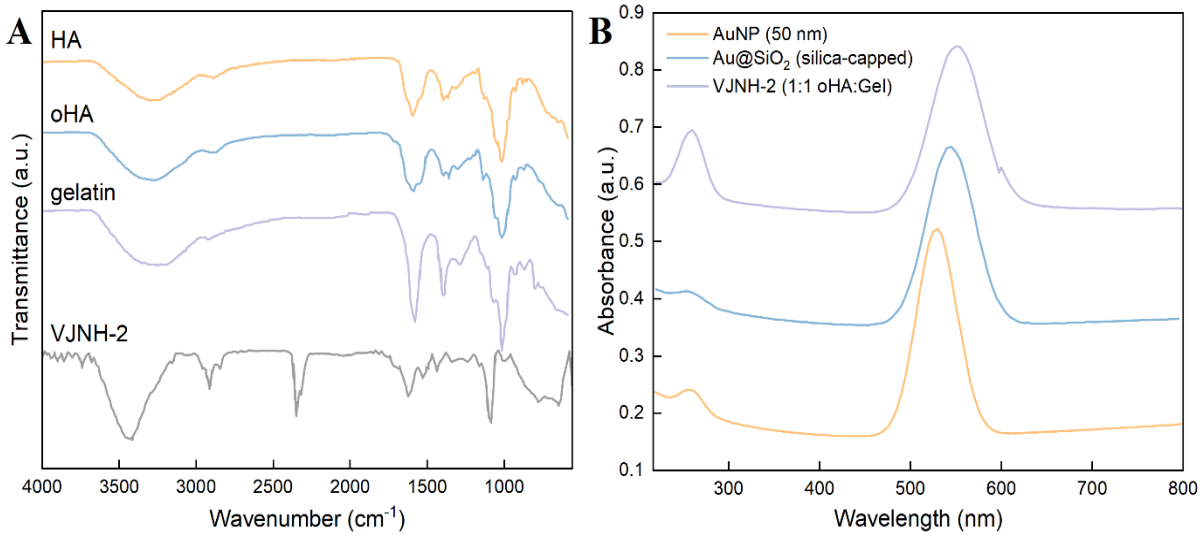

Figure 2. Spectroscopic confirmation of chemistry and asymmetry. (A) FT-IR: appearance of the oHA aldehyde shoulder (~1730 cm^{-1}) and emergence of the imine (C=N) contribution (~1655 cm^{-1}) in VJNH-2 indicating dynamic Schiff-base formation. (B) UV–vis: Au plasmon red-shift (530 → 545 → ~552 nm) from AuNP→Au@SiO_2→VJNH-2 and the 260 nm nucleic-acid band confirming aptamer grafting

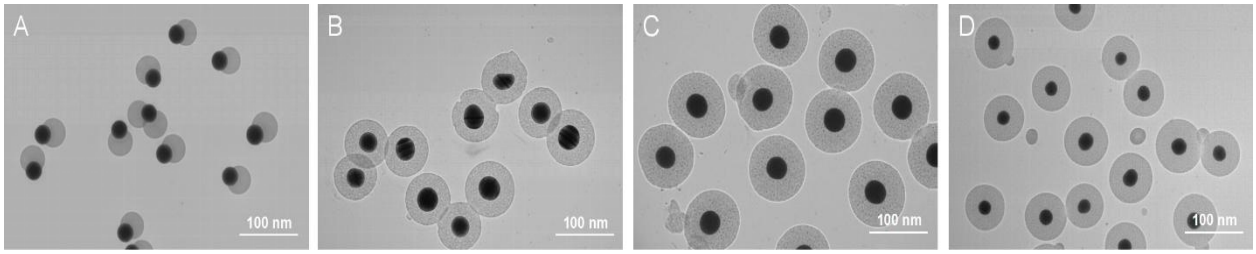

Figure 3. TEM images showing morphology and shell thickness control. (A) Au@SiO_2 "acorn-like" Janus cores (50 nm Au, ~70 nm SiO_2 cap). (B–D) Final VJNHs with low-contrast hydrogel halos: VJNH-1 (~20 nm shell), VJNH-2 (~40 nm), VJNH-3 (~60 nm)

The morphology of the nanoparticles at different synthetic stages was visualized by TEM. Fig. 3 presents TEM images of the Janus cores and the final VJNH formulations. The Au@SiO_2 cores (Fig. 3A) clearly show the asymmetric, "acorn-like" Janus morphology, with a high-contrast, electron-dense 50 nm AuNP partially embedded in a lower-contrast, 70 nm silica cap [37]. The TEM images of the final VJNHs (Figs. 3B-D) show these inorganic cores enveloped within a diffuse, low-contrast "halo," which is characteristic of a highly hydrated hydrogel shell [38]. A clear trend was observed: the thickness of the hydrogel shell correlated directly with the oHA:Gelatin ratio used in the synthesis. VJNH-1 (1:2 ratio) exhibited a thin shell of ≈ 20 nm, VJNH-2 (1:1 ratio) a medium shell of ≈ 40 nm, and VJNH-3 (2:1 ratio) the thickest shell at ≈ 60 nm. This demonstrates that the nanostructure dimensions can be rationally tuned by simple adjustment of the biopolymer precursor concentrations.

EDS elemental mapping provided definitive proof of the Janus architecture. The SEM image of VJNH-2 (Fig. 4A) reveals generally spherical particles with a somewhat porous surface texture. The corresponding EDS maps (Figs. 4B-F) are the most critical evidence for the asymmetric design. The elemental map for gold (Au, Fig. 4B) and silicon (Si, Fig. 4C) are spatially segregated and clearly anti-correlated, confirming the Janus nature of the inorganic core. Furthermore, the maps for carbon (C, Fig. 4D), nitrogen (N, Fig. 4E), and oxygen (O, Fig. 4F) are shown to be co-localized with the silica cap and envelop the entire particle. This strongly indicates that the hydrogel shell preferentially grafts to the functionalized silica face, leaving the aptamer-coated gold face more exposed.

XPS analysis was performed to confirm the surface chemical composition and asymmetry. The survey spectrum of VJNH-2 (Fig. 5A) confirmed the presence of all expected elements: Au, Si, O, C, and N. High-resolution scans (Figs. 5B-D) provided chemical state information. The Au 4f spectrum (Fig. 5B) showed the characteristic Au $4f_{7/2}$ and $4f_{5/2}$ doublet at 84.0 eV and 87.7 eV, respectively, confirming metallic gold. The Si 2p spectrum (Fig. 5C) showed a single peak at 103.5 eV, consistent with SiO_2 [39]. The high-resolution N 1s spectrum (Fig. 5D) was particularly insightful. It was deconvoluted into two primary components: a major peak at 400.0 eV, corresponding to the C-N bonds in the gelatin amide and aptamer bases [40], and a distinct, lower-binding-energy peak at ≈ 399.5 eV. This secondary peak is assigned to the C=N imine bond, providing direct, surface-sensitive evidence of the successful Schiff base crosslinking at the particle surface.

10.57647/jnsc.2026.1603.14

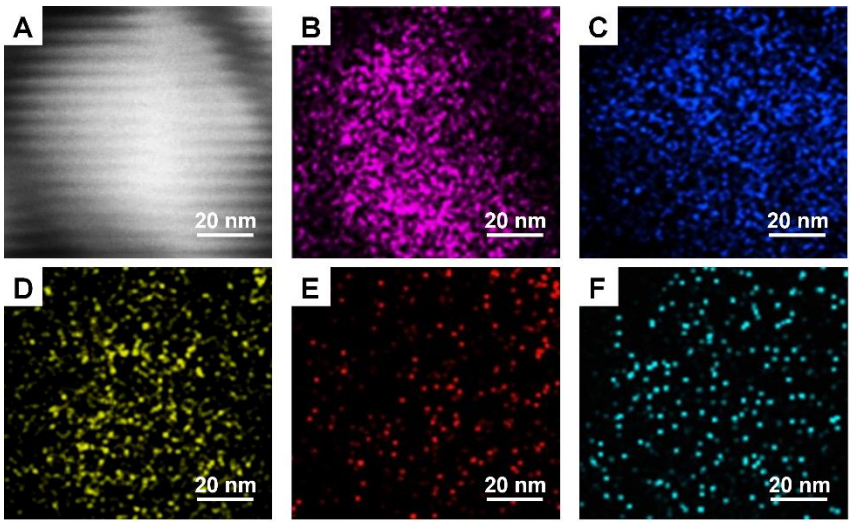

Figure 4. (A) SEM image showing spherical particles with a porous surface morphology. EDS elemental maps confirming the asymmetric Janus structure: (B) Au localized on one hemisphere, (C) Si distributed on the opposite side, and (D–F) C, N, and O co-localized with the Si-rich region, indicating the hydrogel shell grafted preferentially onto the silica face while the Au surface remains exposed

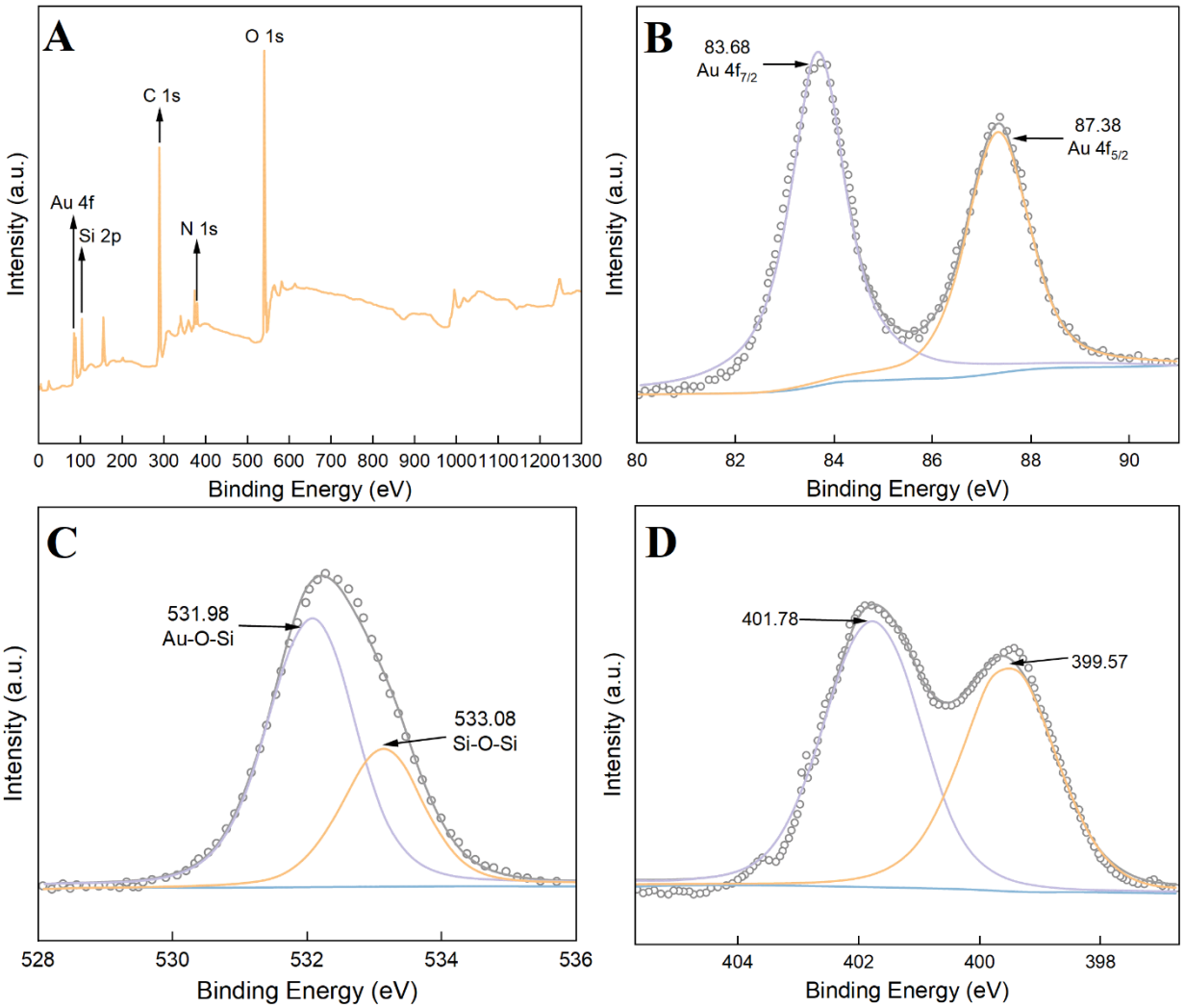

Figure 5. XPS analysis of VJNH-2. (A) Survey spectrum (Au, Si, O, C, N). (B) Au 4f doublet at ~84.0/87.7 eV (metallic Au). (C) Si 2p at ~103.5 eV (SiO_2). (D) N 1s deconvolution showing amide/amine (~400.0 eV) and imine (C=N, ~399.5 eV) components, confirming surface Schiff-base crosslinks

The colloidal properties of the VJNHs were assessed by DLS and zeta potential measurements (Fig. 6 and Table 1). The DLS size distributions (Fig. 6A) showed that all formulations were monodisperse, with polydispersity indices (PDI) below 0.2. The measured hydrodynamic diameters (D_h) *were larger than the TEM dry-state sizes, as expected for hydrated hydrogels. The* D_h trend mirrored the TEM results: VJNH-1 (210.4 nm) < VJNH-2 (245.8

10.57647/jnsc.2026.1603.14

nm) < VJNH-3 (290.1 nm), confirming that a higher oHA:Gelatin ratio leads to a larger hydrated particle. The HNH control, lacking the dense core, had a D_h of 230.5 nm. Zeta potential measurements (Fig. 6B) at pH 7.4 showed that all formulations were highly anionic, with surface charges ranging from -30.7 mV to -34.2 mV. This strong negative charge is attributed to the deprotonation of the abundant carboxylic acid groups on both HA and gelatin at physiological pH [29], and is sufficient to ensure excellent colloidal stability by preventing aggregation.

3.2. Structural, Thermal, and Porosity Analysis

The crystalline and amorphous nature of the VJNH components was investigated by XRD (Fig. 7). The XRD pattern of the precursor AuNPs exhibited sharp diffraction peaks at 2θ = 38.2°, 44.4°, 64.6°, and 77.5°, corresponding to the (111), (200), (220), and (311) planes of the face-centered cubic (fcc) lattice of crystalline gold. The pattern for the final VJNH-2 nanocomposite clearly shows these same crystalline Au peaks superimposed upon a broad, diffuse halo centered at 2θ ≈ 22° [41]. This characteristic broad peak, or "amorphous halo," is the signature of non-crystalline materials and represents the combined contribution of the amorphous silica cap [42] and the amorphous oHA-gelatin polymer network. To confirm this, the pattern for the HNH control shows only this amorphous halo, completely lacking any crystalline peaks. This confirms the successful integration of the crystalline metallic core within the amorphous hydrogel-silica matrix.

Thermal stability and composition were assessed by TGA and DSC (Fig. 8). The TGA curves (Fig. 8A) revealed a multi-stage degradation process for all hydrogel-containing samples. An initial weight loss of 10–15% below 150 °C was observed, corresponding to the evaporation of physically adsorbed and bound water [43]. The primary polymer degradation occurred in the range of 200–350 °C [44]. A clear trend in thermal stability was observed: VJNH-3 (onset ≈ 280 °C) > VJNH-2 (onset ≈ 265 °C) > VJNH-1 (onset ≈ 240 °C). This directly links increased crosslink density (higher oHA ratio) to enhanced thermal stability. A critical distinction was the final residual mass at 800 °C: the VJNH samples all retained ≈ 25% of their initial mass, corresponding to the thermally stable inorganic Au@SiO_2 core. In contrast, the HNH control degraded almost completely, leaving <5% residue. This provides a quantitative, independent measure of the inorganic core loading. The DSC curves (Fig. 8B) showed a broad endotherm peaking around 80–120 °C, confirming the significant water content [45].

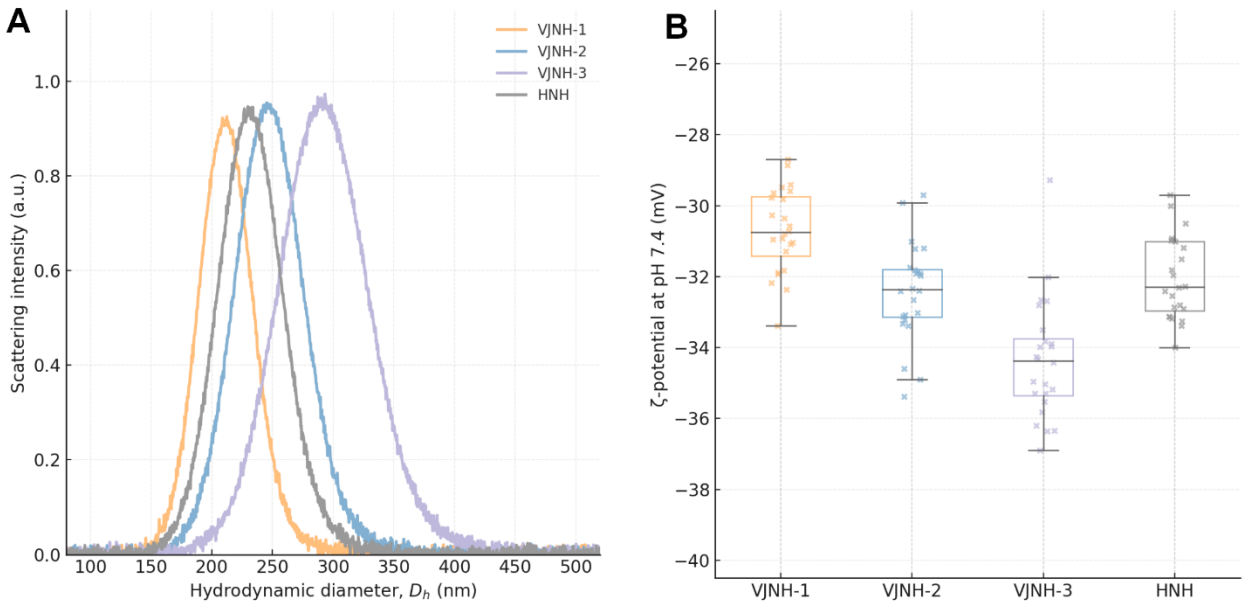

Figure 6. Colloidal characteristics by DLS and ζ-potential at pH 7.4. (A) Narrow, monodisperse size distributions (PDI < 0.2) with hydrodynamic diameters increasing from VJNH-1 < VJNH-2 < VJNH-3; HNH shown for comparison. (B) Strongly anionic ζ-potentials (~−31 to −34 mV) supporting electrostatic stabilization

Table 1. Summary of Colloidal Properties (DLS Hydrodynamic Diameter, PDI, and Zeta Potential) of VJNH Formulations and HNH Control

Sample	oHA:Gelatin Ratio (w/w)	D_h (nm) ± SD	PDI ± SD	Zeta Potential (mV) ± SD
VJNH-1	1:2	210.4 ± 3.1	0.18 ± 0.02	-30.7 ± 1.4
VJNH-2	1:1	245.8 ± 2.8	0.15 ± 0.01	-32.5 ± 1.1
VJNH-3	2:1	290.1 ± 4.5	0.19 ± 0.02	-34.2 ± 1.6
HNH	1:1	230.5 ± 3.3	0.17 ± 0.01	-31.8 ± 1.3

10.57647/jnsc.2026.1603.14

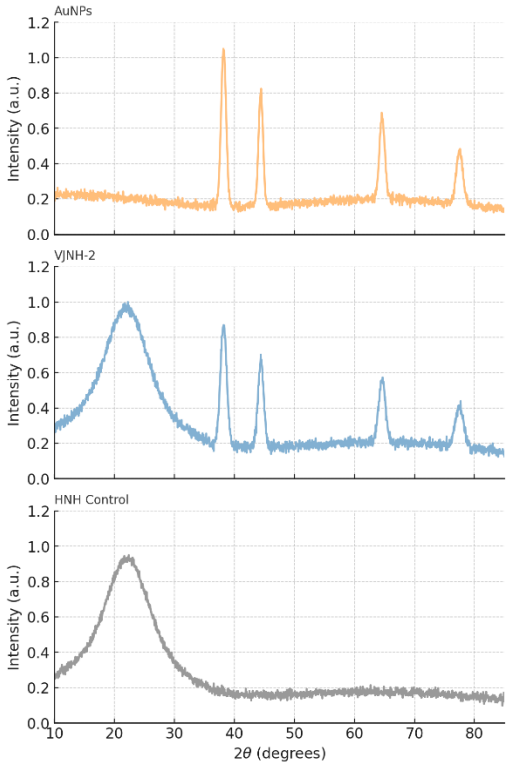

Figure 7. XRD patterns of AuNPs, VJNH-2 and HNH control

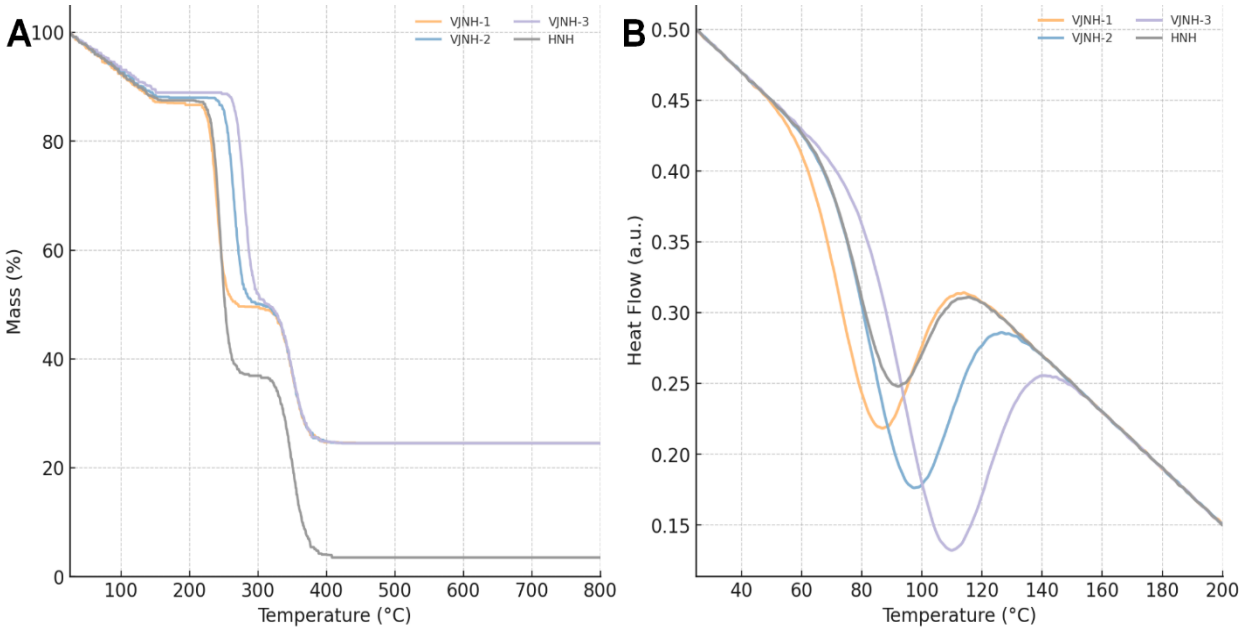

Figure 8. (A) TGA showing initial water loss (<150 °C), polymer degradation (200–350 °C), and residual mass ~25 % at 800 °C for VJNHs due to inorganic cores (HNH < 5 %). (B) DSC with broad endotherm (80–120 °C) consistent with high water content; higher oHA ratio shifts stability

The porosity of the nanostructures was quantified by N_2 adsorption-desorption analysis (Fig. 9). The isotherms for all VJNH formulations (Fig. 9A) were classified as Type IV with a distinct H3-type hysteresis loop. This behavior is the hallmark of mesoporous materials. Conversely, the HNH control showed negligible N_2 uptake, confirming that the dried biopolymer network itself is non-porous. This demonstrates that the observed mesoporosity is an intrinsic property of the silica cap, likely formed during the calcination step which removes the CTAB template [46]. The BJH pore size distribution plot (Fig. 9B) for VJNH-2 revealed a primary pore diameter centered at ≈ 15 nm. This high-surface-area, porous structure is a crucial feature, as it provides diffusion channels for cytokines to reach the binding sites and for encapsulated drugs to be released. The quantitative porosity data are summarized in Table 2. An important structure-property relationship was revealed: the BET surface area decreased as the hydrogel shell thickness increased, from 210.5 m^2/g for VJNH-1 down to 160.3 m^2/g for VJNH-3.

10.57647/jnsc.2026.1603.14

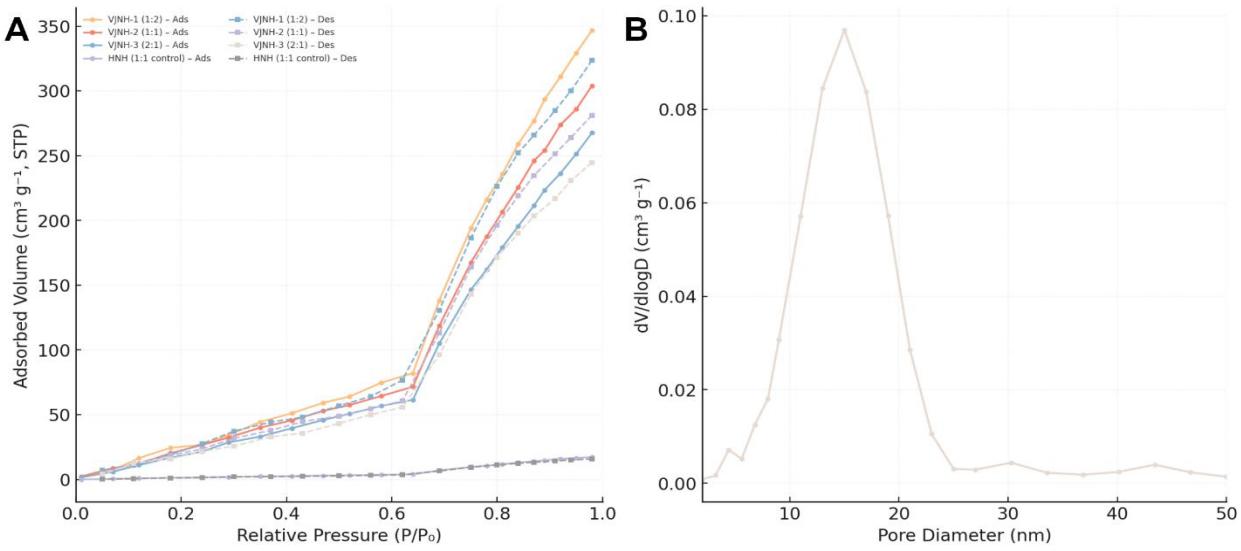

Figure 9. (A) Type IV isotherms with H3 hysteresis for VJNHs, indicating mesoporosity from the silica cap; negligible uptake for HNH. (B) BJH pore size distribution centered around ~15 nm (VJNH-2)

Table 2. BET Surface Area, Total Pore Volume, and Average Pore Diameter of VJNH Formulations and HNH Control

Sample	BET Surface Area (m^2/g)	Total Pore Volume (cm^3/g)	Avg. Pore Diameter (nm)
VJNH-1	210.5 ± 8.2	0.78 ± 0.03	14.8
VJNH-2	185.3 ± 6.5	0.70 ± 0.02	15.1
VJNH-3	160.3 ± 7.1	0.61 ± 0.03	15.2
HNH	8.7 ± 1.3	0.01 ± 0.00	N/A

This strongly suggests that the thicker, denser hydrogel shell of VJNH-3 partially obstructs the openings of the silica mesopores, reducing the accessible surface area. This represents a critical design trade-off between shell thickness and pore accessibility.

3.3. Viscoelastic Properties and Swelling Behavior

The defining viscoelastic property of the hydrogel network was quantified using bulk rheology on gels prepared with equivalent polymer compositions. Oscillatory frequency sweeps (Fig. 10A) showed $G' > G''$ across 0.1–100 rad s^{-1} for all VJNH formulations, confirming solid-like gel behavior while the non-negligible, frequency-dependent loss response indicates a viscoelastic solid rather than an ideal elastic network. A clear compositional trend was observed: stiffness (G' at 10 rad s^{-1}) increased with crosslink density from ≈150 Pa (VJNH-1) to ≈300 Pa (VJNH-2) and ≈550 Pa (VJNH-3), demonstrating tunability within the mechanically compliant regime relevant to injectable, matrix-mimetic hydrogels. Importantly, these values fall within the stiffness window commonly reported for injectable hydrogels crosslinked by dynamic covalent chemistries, where G' can span approximately 10–1000 Pa depending on functionalization and polymer architecture, enabling extrusion while maintaining post-injection integrity. In related hydrazone-linked HA/protein DCC systems, storage moduli on the order of 1000 Pa are achieved at similar polymer weight fractions, and can be reduced by small-molecule modulation over orders of magnitude, illustrating that our 150–550 Pa range is consistent with the broader DCC design space while remaining intentionally softer for diffusion-permissive, viscoelastic shells. The complex viscosity (Fig. 10B) decreased with increasing angular frequency, confirming shear-thinning behavior that supports injectability and is expected for transiently crosslinked networks [47]. Stress-relaxation tests (Fig. 11A) further clarified the origin and timescale of viscoelasticity. Under a constant strain, stress relaxed over time, consistent with bond exchange and network rearrangement of reversible imine linkages. The relaxation time increased with crosslink density ($\tau \approx 60$ s for VJNH-1, ≈ 120 s for VJNH-2, and ≈ 180 s for VJNH-3), indicating slower chain mobility and fewer available rearrangement pathways in denser networks [16]. Notably, these relaxation times are comparable to the tens-to-hundreds-of-seconds stress-relaxation regimes reported to be biologically consequential in stress-relaxing hydrogels, where changing relaxation time from ~70 s to ~170 s alters cell spreading and proliferation in 3D matrices. This alignment supports our interpretation that the VJNH shell is not only mechanically tunable but also dynamically remodelable on ECM-relevant timescales. Consistent with this dynamic exchange mechanism, VJNH-2 exhibited macroscopic self-healing within 1 h at 37 °C, reflecting spontaneous reformation of reversible C=N linkages at the interface [22].

10.57647/jnsc.2026.1603.14

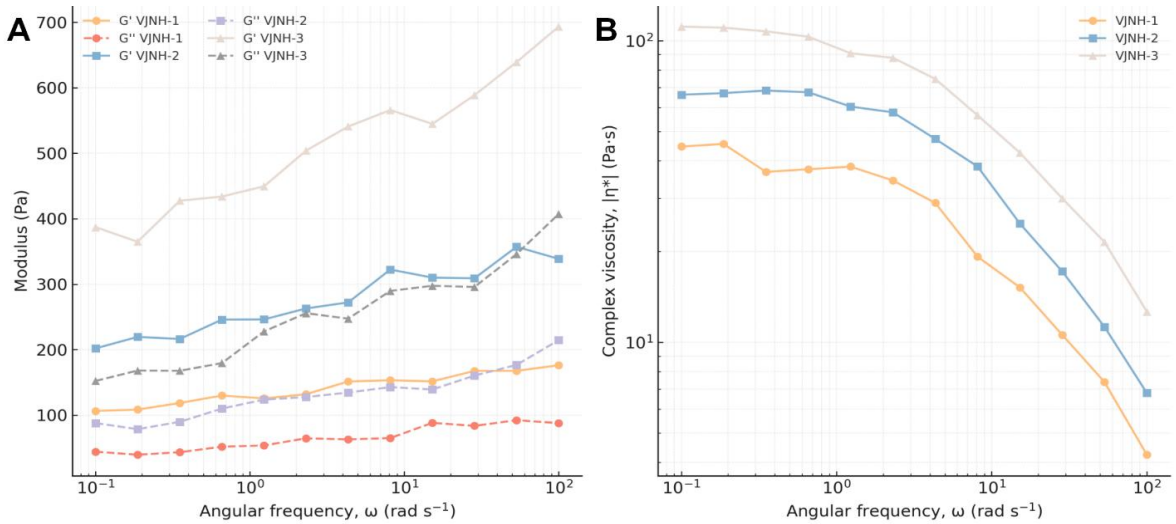

Figure 10. (A) Frequency sweeps: G′ > G″ over 0.1–100 rad s⁻¹; stiffness tunable with composition (VJNH-1 < VJNH-2 < VJNH-3). (B) Complex viscosity vs angular frequency showing shear-thinning behavior favorable for injectability

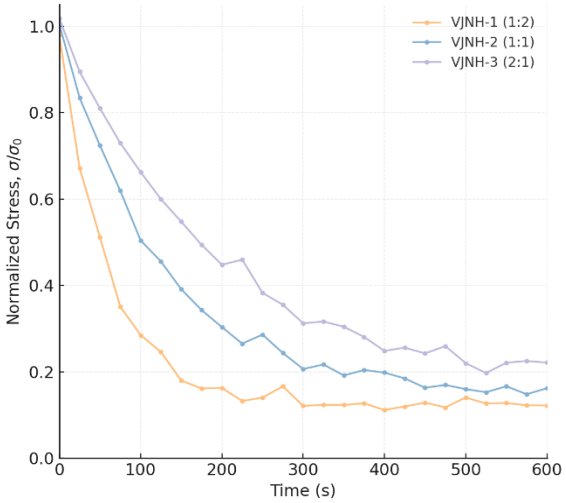

Figure 11. Viscoelastic relaxation and macroscopic self-healing. (A) Stress-relaxation curves with relaxation times ~60 s (VJNH-1), ~120 s (VJNH-2), ~180 s (VJNH-3), reflecting dynamic imine bond exchange

The "smart" behavior of the nanohydrogels was investigated through pH-dependent swelling studies (Fig. 12, and Table 3). All VJNH formulations exhibited strong pH-responsiveness. The Equilibrium Swelling Ratio (ESR) at physiological pH 7.4 was significantly higher than in an acidic environment (pH 5.5) (Fig. 12A). For VJNH-2, the ESR was ≈ = 1200% at pH 7.4 but only ≈ 700% at pH 5.5. This behavior is governed by the ionization state of the carboxylate groups (-COO^-) on both HA and gelatin, which have a pKa of ≈ 3-4 [29]. At pH 7.4, these groups are fully deprotonated, leading to strong intramolecular and intermolecular electrostatic repulsion. This repulsion forces the polymer chains apart, causing the hydrogel network to expand and imbibe large amounts of water. At pH 5.5, this repulsion is partially shielded, leading to a more collapsed network.

The swelling kinetics (Fig. 12B) showed that equilibrium was reached within ≈ 12 hours. An important structure-property trade-off was identified: the swelling capacity was inversely correlated with mechanical stiffness. The softest gel, VJNH-1, showed the highest swelling, while the stiffest gel, VJNH-3, showed the lowest. This quantitative relationship between composition, stiffness, and swelling is summarized in Table 3.

3.4. Biocompatibility and Performance Evaluation

The cytocompatibility of the VJNH platform is a prerequisite for any biomedical application. An extract-based MTT assay using L929 fibroblast cells was perfoty of soluble/leachable components from the VJNH formulations (Fig. 13), using clarified, sterile-filtered eluates prepared at 37 °C for 24 h. After 24, 48, and 72 h of incubation (Figs. 13A–C), cell viability remained above 90% for all VJNH formulations at all tested equivalent extract concentrations (0.1–1.0 mg/mL). These results, which are comparable to the untreated media control, demonstrate that the VJNHs are non-cytotoxic and that the synthesis and purification protocols effectively remove any residual unreacted precursors, such as glutaraldehyde or $NaIO_4$ [30].

10.57647/jnsc.2026.1603.14

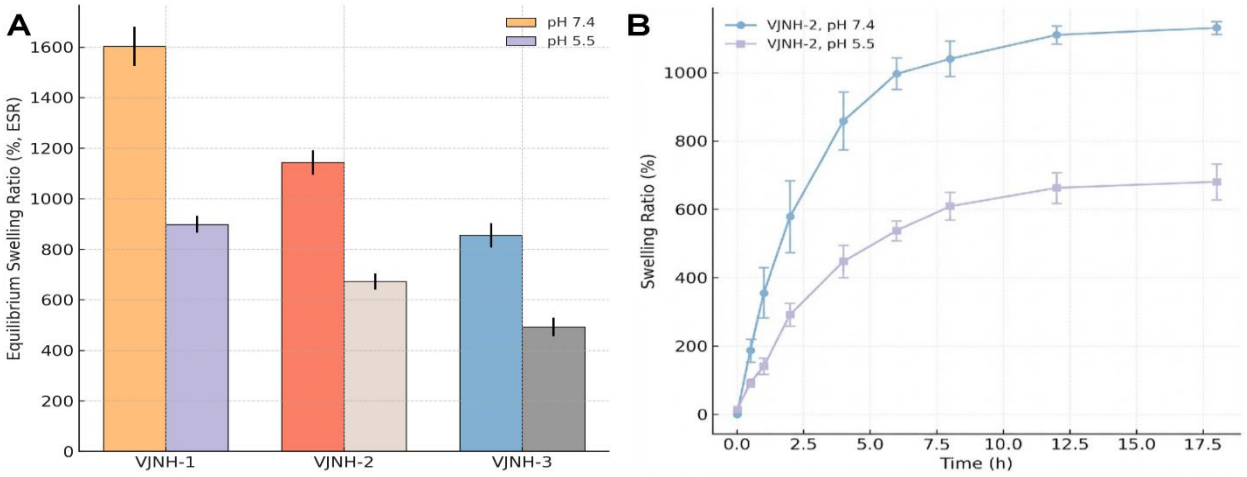

Figure 12. pH-responsive swelling. (A) Equilibrium swelling ratio (ESR) markedly higher at pH 7.4 than pH 5.5 for all formulations; trade-off between stiffness and swelling. (B) Swelling kinetics reaching equilibrium within ~12 h

Table 3. Summary of Key Rheological and Swelling Properties for VJNH Formulations

Sample	G′ at 10 rad/s (Pa)	Relaxation Time, τ (s)	ESR at pH 7.4 (%)	ESR at pH 5.5 (%)
VJNH-1	150 ± 12	60 ± 5	1550 ± 80	910 ± 50
VJNH-2	300 ± 18	120 ± 10	1200 ± 65	700 ± 40
VJNH-3	550 ± 25	180 ± 15	850 ± 50	520 ± 30

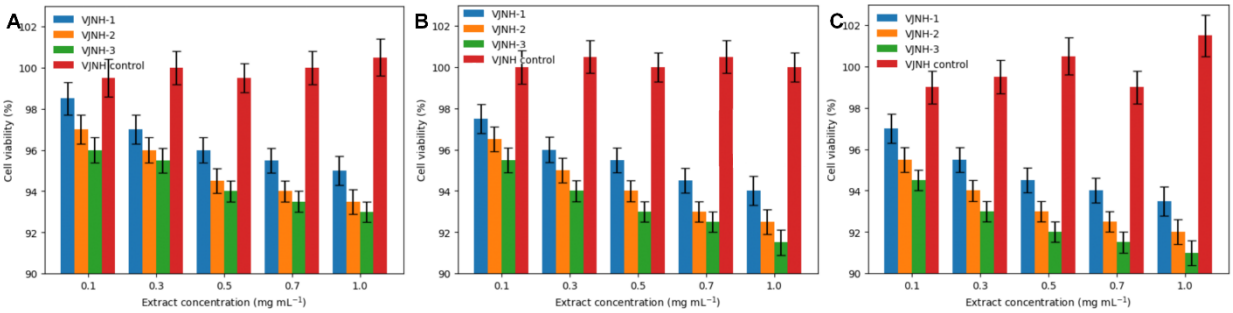

Figure 13. Cytocompatibility by MTT assay on L929 fibroblasts. Cell viability remains >90 % across 0.1–1.0 mg mL⁻¹ extract concentrations at (A) 24, (B) 48, (C) 72 h for all VJNH formulations, comparable to untreated controls

The primary function of the VJNHs, IL-1β sequestration, was first evaluated using an ELISA-based depletion assay (Fig. 14). When incubated in a 500 pg/mL solution of IL-1β (Fig. 14A), all three aptamer-functionalized VJNH formulations rapidly sequestered the cytokine. The VJNH-2 formulation, for example, depleted over 90% of the free IL-1β from the solution within 8 hours. In sharp contrast, the two control samples showed minimal binding, with <20% depletion even after 24 hours. This minimal uptake is attributed to non-specific physisorption. The significant difference between the VJNHs and the controls provides definitive proof that the sequestration is rapid, efficient, and, most importantly, aptamer-driven. The specificity of this interaction was confirmed in a competitive binding assay (Fig. 14B). When VJNH-2 was incubated in a cocktail of IL-1β, TNF-α, and BSA, it selectively depleted IL-1β while showing no significant binding of the other two proteins.

While all VJNHs were effective, their equilibrium binding capacities (q_e; ng IL-1β per mg nanohydrogel) were compared to identify an optimal sequestration formulation (Fig. 15). This comparison revealed a non-linear "sweet spot" relationship: VJNH-1 (1:2; lowest stiffness, highest swelling) showed $q_e \approx 120$ ng/mg, VJNH-3 (2:1; highest stiffness, lowest swelling) showed $q_e \approx 150$ ng/mg, and VJNH-2 (1:1) achieved the highest capacity ($q_e \approx 180$ ng/mg).

Importantly, in this study the formulation-dependent 'mechanical integrity' is supported indirectly by bulk viscoelastic metrics (G′ and stress-relaxation time, τ) and swelling (ESR) rather than by tensile/compressive failure testing. We therefore interpret the VJNH-1 vs VJNH-3 differences primarily as a transport–mechanics trade-off: the softer, highly swollen network (VJNH-1) may be less resistant to handling/deformation, whereas the denser, highly crosslinked network (VJNH-3; higher G′, lower ESR) can reduce protein accessibility by increasing steric/mesh constraints and limiting diffusion to internal aptamer sites.

Based on its superior binding capacity together with intermediate viscoelasticity and swelling, VJNH-2 was selected for subsequent kinetic studies.

10.57647/jnsc.2026.1603.14

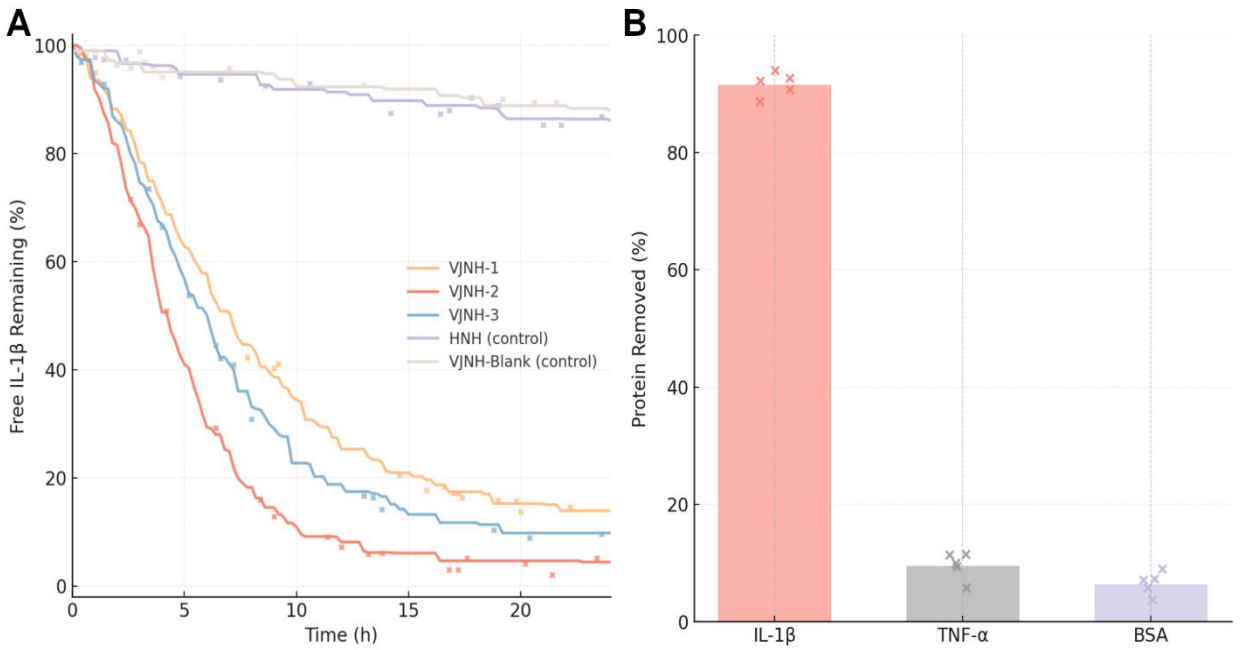

Figure 14. (A) Depletion kinetics from 500 pg mL^{-1} IL-1β: fast, high-efficiency capture by VJNHs (VJNH-2 removes >90 % by 8 h) vs minimal uptake by HNH and VJNH-Blank. (B) Specificity in a protein cocktail (IL-1β, TNF-α, BSA): selective removal of IL-1β only

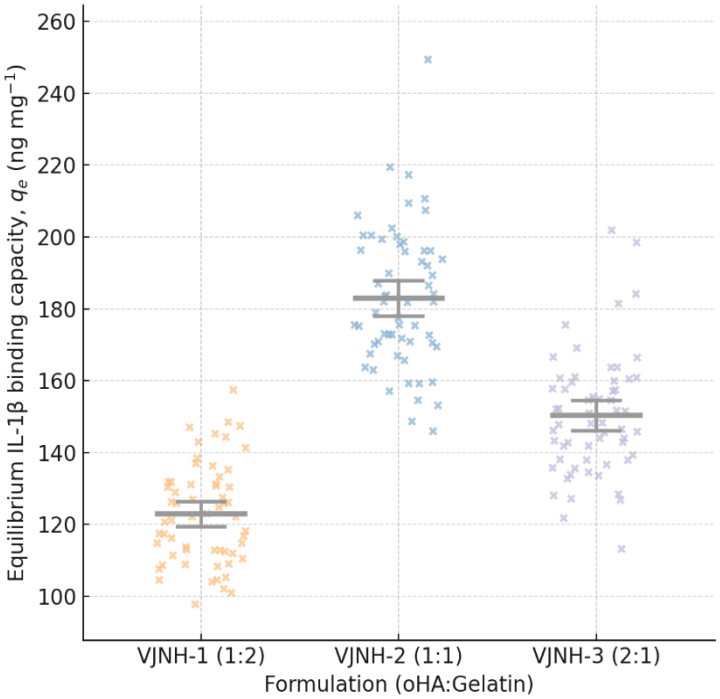

Figure 15. Equilibrium IL-1β binding capacity (q_e) comparison. Non-linear trend with composition; VJNH-2 (1:1 oHA:Gelatin) achieves the highest capacity (~180 ng mg^{-1}), outperforming softer VJNH-1 and stiffer VJNH-3

Real-time binding kinetics of VJNH-2 with IL-1β were quantified by SPR (Fig. 16 and Fig. 17). The sensorgrams (Fig. 16A) from multi-cycle kinetic analysis, using IL-1β concentrations from 1.25 nM to 20 nM, show the classic, concentration-dependent association and dissociation curves [48]. The curves were fitted to a 1:1 Langmuir binding model (Fig. 16B), which showed an excellent goodness-of-fit, indicating a well-behaved, monovalent-like binding interaction. The steady-state affinity plot (Fig. 17A) further confirms this strong interaction. An SPR-based specificity test (Fig. 17B) reinforced the ELISA findings: injection of 50 nM IL-1β produced a strong binding response (≈ 120 RU), whereas injections of 50 nM TNF-α and 50 nM BSA produced no signal, confirming the high fidelity of the aptamer-based recognition.

The quantitative kinetic constants derived from the SPR analysis are presented in Table 4. The VJNH-2 platform demonstrated a rapid association rate (k_{on}) of 2.5 × 10^5 M^{-1}s^{-1} and, crucially, a very slow dissociation rate (k_{off}) of 3.1 × 10^{-4} s^{-1}. This slow off-rate is highly desirable for a sequestration agent, as it implies that once

10.57647/jnsc.2026.1603.14

the IL-1β cytokine is captured, it is held for a long duration. The equilibrium dissociation constant (K_D), calculated as k_{off} / k_{on}, was determined to be 1.24 nM [49]. This value represents an exceptionally high binding affinity, well within the range of therapeutic monoclonal antibodies [50], and confirms the VJNH-2 platform as a highly efficient and potent sequestration device. The VJNH-Blank control showed no measurable binding in the SPR analysis.

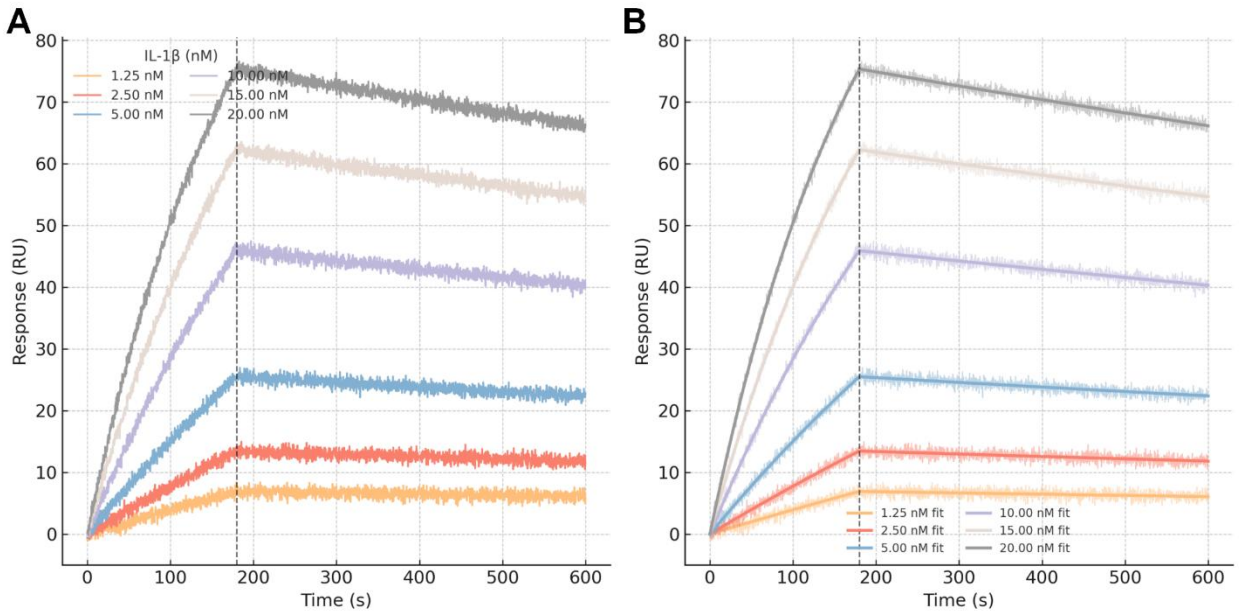

Figure 16. SPR multi-cycle kinetics for VJNH-2–IL-1β binding. (A) Concentration-dependent sensorgrams (1.25–20 nM). (B) Global fits to a 1:1 Langmuir model indicating rapid association and slow dissociation

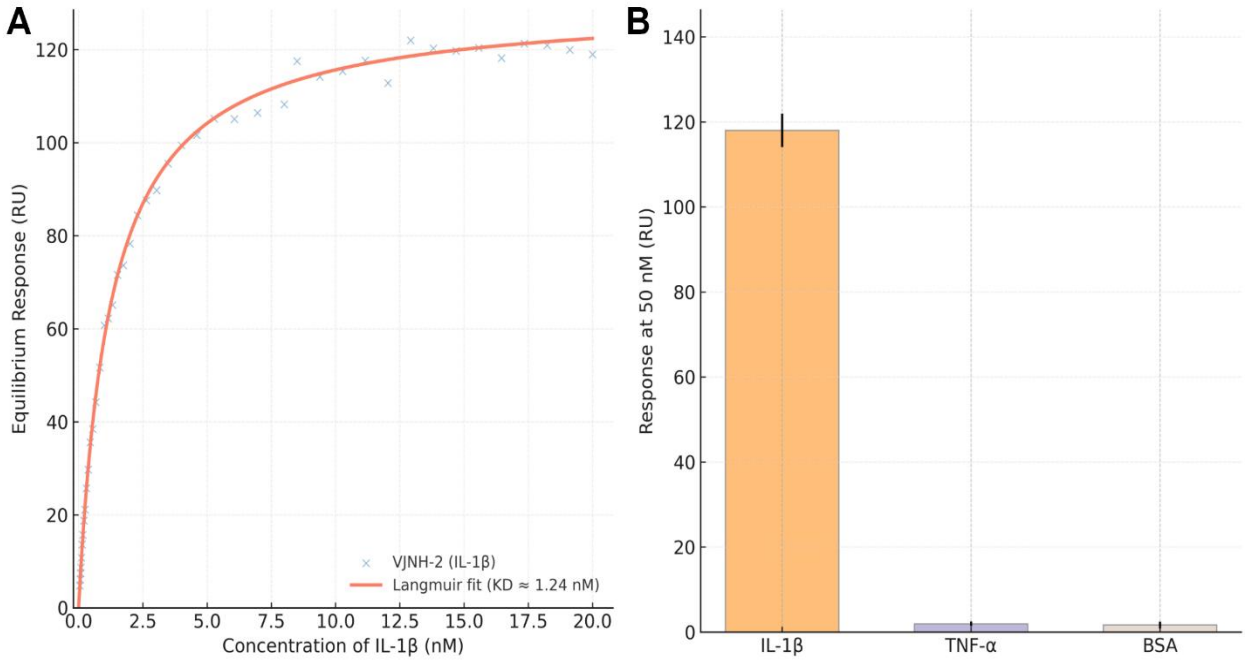

Figure 17. SPR steady-state affinity and specificity. (A) Equilibrium binding isotherm for VJNH-2 yielding sub-nanomolar to low-nanomolar affinity (K_D ≈ 1.24 nM). (B) Control injections of TNF-α and BSA show no response, confirming selective IL-1β recognition

Table 4. Summary of IL-1β Binding Kinetics and Affinity for VJNH-2 and VJNH-Blank, Determined by SPR

Sample	Analyte	k_{on} ($M^{-1}s^{-1}$)	k_{off} (s^{-1})	KD (nM)
VJNH-2	IL-1β	2.5×10^5	3.1×10^{-4}	1.24
VJNH-2	TNF-α	N.B.	N.B.	N.D.
VJNH-2	BSA	N.B.	N.B.	N.D.
VJNH-Blank	IL-1β	N.B.	N.B.	N.D.

10.57647/jnsc.2026.1603.14

3.5. Therapeutic Release Kinetics

Finally, the dual-function capability of the VJNHs was tested by evaluating the release of a model anti-inflammatory drug, DEX, encapsulated within the viscoelastic shell (Fig. 18). Unless otherwise stated, DEX was loaded at 10% w/w relative to total polymer, a level chosen based on preliminary optimization (5–20% w/w) to ensure formulation stability and to avoid conditions that may promote excessive early burst ('dose dumping') while maintaining measurable sustained release suitable for mechanistic modeling.

All formulations provided sustained release of DEX over 72 hours, with no significant burst release under the tested conditions, indicating stable encapsulation in the selected formulation window. Two major trends were evident. First, the release rate was dependent on the hydrogel crosslink density. The softest gel, VJNH-1, released its cargo fastest (≈ 90% at 48h), while the stiffest gel, VJNH-3, provided the most sustained release (≈ 60% at 72h). This is because the denser, less-swollen network of VJNH-3 creates a more tortuous diffusion path for the drug.

Second, release was pH-responsive. For VJNH-2, cumulative DEX release was faster at physiological pH 7.4 (≈80% at 72 h) than under mildly acidic conditions (pH 5.5; ≈55% at 72 h). This directionality is consistent with our swelling data (Fig. 12, Table 3), and indicates that diffusion through the hydrogel mesh is the dominant pH-sensitive control lever in this system. At pH 7.4, deprotonation of HA-associated carboxyl groups increases fixed negative charge density and electrostatic repulsion, which expands the network and increases water uptake, thereby increasing effective diffusivity and accelerating release.

Conversely, at lower pH, reduced ionization leads to partial network collapse, smaller mesh size, and slower solute transport. This mechanism aligns with established pH-sensitive hydrogel principles in which ionization state governs swelling and permeability, and it is also consistent with hyaluronan hydrogel studies highlighting charge-driven swelling changes [51].

We also note that pH-responsive DCC hydrogels are frequently discussed in the context of acid-labile Schiff-base bond cleavage, which can accelerate degradation and cargo release in more acidic environments [52]. In our VJNH system, the observed slower release at pH 5.5 suggests that, over the 72 h window and under the tested conditions, ionization-controlled swelling and diffusion outweigh any acid-accelerated imine cleavage. This distinction is important because it implies the release trigger is primarily a reversible permeability switch rather than rapid network breakdown, which may be advantageous when prolonged local dosing is desired. Taken together with the Higuchi/Korsmeyer–Peppas fits, these comparisons clarify that our pH response is best interpreted as a swelling-modulated, diffusion-controlled release process rather than a degradation-dominated mechanism.

To elucidate the release mechanism, the data were fitted to mathematical models (Fig. 19A-B, and Table 5). The release data for the first 60% of release showed an excellent linear fit ($R^2 > 0.99$) to the Higuchi model (Q vs. $t^{1/2}$) (Fig. 19A), which is characteristic of a release mechanism governed by Fickian diffusion from a matrix. This was further confirmed by fitting the data to the Korsmeyer-Peppas model ($\log(M_t/M\infty)$) vs. log t) (Fig. 19B) [33]. This model is described by the equation $(M_t/M\infty) = Kt^n$, where 'n' is the release exponent, a value that indicates the transport mechanism [53]. For a spherical matrix, an 'n' value of ≈ 0.43 indicates pure Fickian diffusion. As shown in Table 5, the calculated 'n' values for all VJNH formulations under both pH conditions were in the range of 0.47–0.49.

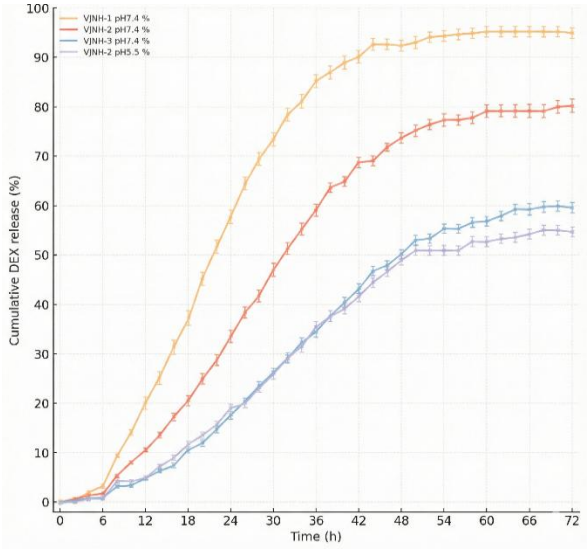

Figure 18. DEX release profiles. Sustained release over 72 h with rate governed by crosslink density at pH 7.4 (VJNH-1 fastest; VJNH-3 slowest) and pH-dependent release for VJNH-2 (faster at pH 7.4 than 5.5) consistent with swelling behavior

10.57647/jnsc.2026.1603.14

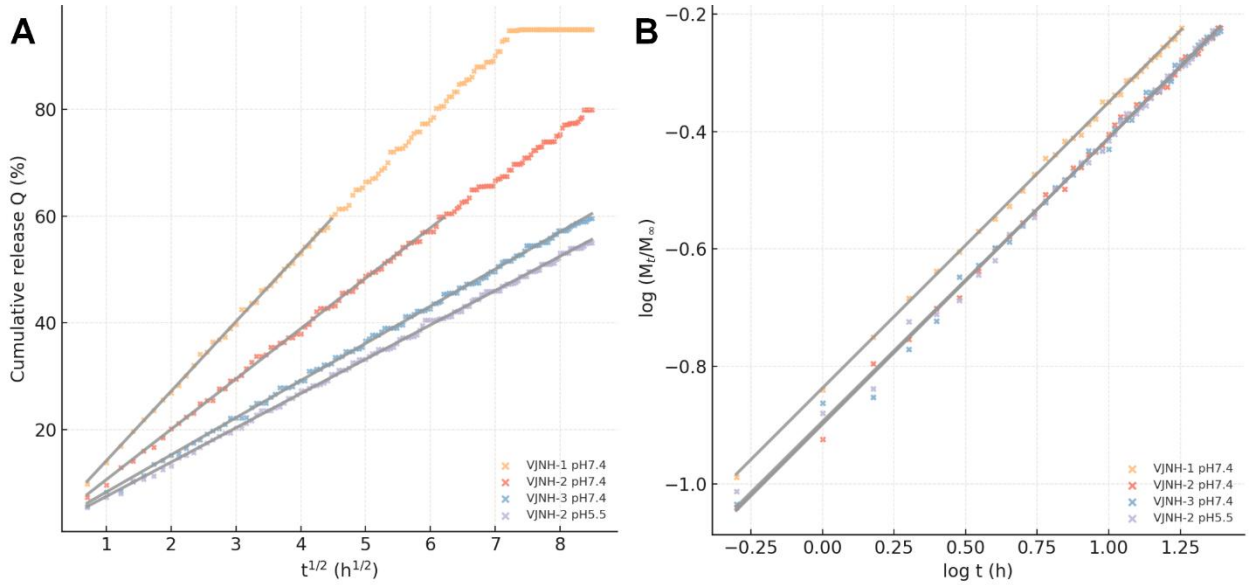

Figure 19. (A) Higuchi model fits for DEX release (Q vs $t^{1/2}$). Linear behavior ($R^2 > 0.99$ for the first ~60 % release) indicates Fickian diffusion from the VJNH matrix dominates transport. (B) Korsmeyer–Peppas analysis (log M_t/M_∞ vs log t) for DEX release. Release exponents n ≈ 0.47–0.49 across formulations and pH conditions, corroborating Fickian diffusion-controlled release

Table 5. Release Kinetic Parameters and Goodness-of-Fit (R^2) from Higuchi and Korsmeyer-Peppas Models for DEX Release

Sample	pH	Higuchi R^2	Korsmeyer-Peppas R^2	Release Exponent (n)
VJNH-1	7.4	0.994	0.996	0.49
VJNH-2	7.4	0.992	0.995	0.48
VJNH-3	7.4	0.990	0.993	0.47
VJNH-2	5.5	0.990	0.993	0.47

These values are extremely close to the theoretical value for Fickian diffusion, quantitatively confirming that the release of DEX from the VJNHs is diffusion-controlled and not driven by hydrogel erosion or anomalous swelling.

Study limitation and future work: The present release dataset was generated at a single working DEX loading (10% w/w), selected through preliminary formulation optimization to support the platform/mechanism focus of this work. A systematic loading-dependent study (e.g., 5%, 10%, 15%, 20% w/w) is warranted to define a true 'optimal' loading for specific indications by jointly evaluating (i) loading efficiency and physical stability, (ii) early-time burst and long-term release profiles, and (iii) anti-inflammatory efficacy and safety windows in relevant bioassays. Prior studies of corticosteroid delivery systems highlight that burst magnitude and exposure profiles can be sensitive to formulation parameters, underscoring the importance of this planned optimization. Taken together, the depletion/SPR studies establish VJNH-2 as a potent IL-1β 'sink,' and the release experiments establish the hydrogel shell as a sustained DEX reservoir; however, these measurements do not by themselves quantify anti-inflammatory efficacy. Prior work shows that cytokine sequestration matrices can attenuate inflammatory signaling by reducing local cytokine bioavailability, and that localized DEX hydrogels can suppress inflammatory outcomes while reducing systemic exposure. In future work, the dual-action hypothesis can be tested directly by comparing matched formulations in standardized inflammation models, including 'capture only' (aptamer-VJNH without DEX), 'release only' (DEX-loaded VJNH-Blank or non-binding hydrogel), and 'combined' (DEX-loaded aptamer-VJNH), using cytokine outputs (e.g., IL-6/TNF-α), NF-κB pathway readouts, and cell viability; synergy can be evaluated quantitatively using reference additivity models (e.g., Bliss independence).

3.6. Long-term Stability Under Physiological Conditions

Given the dynamic nature of imine crosslinks, we assessed the integrated VJNH-2 nanocomposite stability under physiological aging. In PBS (pH 7.4, 37 °C), VJNH-2 maintained a narrow size distribution over 28 days, with Dh changing modestly from 245.8 nm (day 0; Table 1) to 252–258 nm (day 28), while PDI remained <0.20. In 10% FBS-containing medium, an expected small increase in apparent Dh (to ~265–275 nm by day 7) was observed, consistent with protein adsorption phenomena reported for silica-based nanoparticles, while PDI remained <0.22 and no macroscopic aggregation was detected [54]. ζ-Potential remained strongly negative

10.57647/jnsc.2026.1603.14

throughout incubation (typically within ~3 mV of the initial −32.5 mV), supporting electrostatic stabilization of the dispersion and indicating that prolonged incubation did not induce charge neutralization severe enough to trigger flocculation. TEM images collected after 28 days in PBS showed preservation of the acorn-like Au@SiO_2 Janus core enveloped by the hydrogel halo, with no evidence of core fracture or gross shell detachment. FTIR spectra after aging retained the characteristic imine-associated contribution near ~1655 cm^{-1}, indicating that the dynamic network remained present over the test window; this is consistent with prior reports that Schiff-base hydrogel networks can retain structural signatures during incubation at 37 °C, while exhibiting time-dependent remodeling rather than abrupt disintegration [55]. Functionally, aged VJNH-2 retained IL-1β sequestration performance: after 28 days in PBS, the equilibrium binding capacity remained >85% of the fresh material (q_e ≈ 150–160 ng mg^{-1} versus ≈180 ng mg^{-1} for fresh VJNH-2), indicating that prolonged incubation did not eliminate aptamer-driven capture. Collectively, these results support that the VJNH nanocomposite is stable over multi-week physiological incubation, while still leveraging dynamic imine exchange for viscoelasticity. This balance is important because overly labile dynamic bonds can limit long-term use, whereas appropriately formulated Schiff-base networks can provide both stress relaxation and practical stability under physiological conditions [21]. Additionally, gradual silica dissolution is a known long-term phenomenon for mesoporous silica in physiological environments, but no destabilizing effect was observed within the 28-day window used here [56].

4. Conclusion

In summary, this research details the successful, rational design, and bottom-up synthesis of a novel VJNH platform. This advanced nanocomposite was constructed from an asymmetric Au@SiO_2 inorganic core, which was spatially functionalized with an IL-1β-binding aptamer on the gold face and a viscoelastic hydrogel shell grafted to the silica face. The shell itself was fabricated using dynamic covalent chemistry, specifically the Schiff base linkage formed between oxidized hyaluronic acid and gelatin, imparting biomimetic properties to the material. An exhaustive characterization campaign provided definitive proof of the VJNH structure and properties. High-resolution TEM, SEM, and EDS elemental mapping confirmed the asymmetric Janus architecture. XPS analysis validated the spatially segregated surface chemistry and the formation of the C=N imine bonds. BET analysis confirmed the mesoporous nature of the silica component, which is critical for diffusion. Rheological studies quantified the ECM-mimetic properties of the network, demonstrating that the VJNHs are truly viscoelastic (G' > G"), capable of rapid stress relaxation, and self-healing, all attributable to their dynamic covalent nature. Furthermore, the nanohydrogels were shown to be highly biocompatible via MTT assay.

The optimized VJNH-2 formulation demonstrated exceptional, dual-function performance as a ‘sense-and-respond’ therapeutic platform. The aptamer-functionalized ‘binding face’ proved to be a highly efficient and specific sequestration agent for the pro-inflammatory cytokine IL-1β. This was quantified by a high binding capacity (≈ 180 ng/mg) in ELISA-based assays and an exceptionally strong, antibody-like binding affinity (KD ≈ 1.24 nM) determined by SPR. Concurrently, the viscoelastic hydrogel ‘body’ functioned as a ‘smart’ therapeutic reservoir, providing sustained, pH-responsive, and Fickian diffusion-controlled release of a model anti-inflammatory drug. This dual-action capability—simultaneously removing a key pro-inflammatory driver (IL-1β) while locally releasing an anti-inflammatory agent (DEX)—supports a dual-mechanism, ‘sense-and-respond’ immunomodulation concept. While the current work quantifies high-affinity IL-1β sequestration and sustained DEX release, direct functional comparisons of anti-inflammatory efficacy across ‘capture only,’ ‘release only,’ and ‘combined’ modes will be required to establish additivity or true synergy in cellular or in vivo inflammation models. The VJNH platform represents a significant advance in therapeutic nanomaterials at the interface of nanochemistry and biomedical engineering. By uniquely synergizing spatial control (Janus design) with mechanical biomimicry (viscoelasticity), this work establishes a robust and tunable platform for the development of next-generation therapies.

Future work will prioritize in vivo validation of both biosafety and adaptor stability in disease-relevant settings. First, we will perform local and systemic safety evaluation after periodontal delivery, including hematology/serum biochemistry, inflammatory-marker profiling, and histopathology of major organs, consistent with in vivo biosafety practices commonly reported for injectable hyaluronic-acid-based hydrogels. Second, we will quantify in vivo residence, biodegradation, and potential off-target distribution by labeling the hydrogel phase and independently tracking the Au@SiO_2 core (e.g., fluorescence imaging for the hydrogel and elemental analysis for Au), thereby linking in vivo retention to the diffusion-controlled release behavior established here. Third, we will directly test in vivo stability of the IL-1β aptamer adaptor (nuclease resistance and binding persistence in serum and in vivo). If stabilization is required, we will implement established aptamer-protection strategies (terminal caps and sugar/backbone or PEG modifications) that are routinely used to extend oligonucleotide lifetime and have been validated in

10.57647/jnsc.2026.1603.14

clinically approved aptamer therapeutics, while re-confirming affinity and specificity by SPR using the same kinetic framework reported in this study. Finally, therapeutic efficacy will be assessed in standard ligature-induced periodontitis animal models using micro-CT and histology endpoints for inflammation and bone preservation, which are widely used to benchmark hydrogel-based local periodontal therapies.

Acknowledgements

This work has been supported by Peking University Clinical Medicine + X Youth Special Program. PKU2025PKULCXQ007; Beijing Natural Science Foundation - Haidian Original Innovation Joint Fundation L252167; The Digital Healthcare Proof-of-Concept Program in Chaoyang District 2025SLZZ009.

Author Contributions

L.P., G.Y., and G.W. contributed to the conceptualization and methodology of the study. L.P., G.W., X.Y., and Y.Z. carried out the experiments and investigation. L.P. and G.Y. performed data curation and formal analysis. L.P. and X.Y. contributed to data interpretation and visualization. L.P. wrote the original draft of the manuscript. G.Y., G.W., X.O., and J.Q. reviewed and edited the manuscript. J.Q. and X.O. supervised the research and provided critical intellectual input. J.Q. was responsible for project administration and funding acquisition.

Availability of Data and Materials

The data supporting the findings of this study are available from the corresponding author upon reasonable request.

Conflict of Interest

The authors declare that they have no known competing financial interests or personal relationships that could have appeared to influence the work reported in this paper.

Ethical Approval

All procedures involving human blood samples were conducted in accordance with the ethical standards of the institutional research committee and with the Declaration of Helsinki. The hemolysis assay was performed using blood obtained from a healthy volunteer after informed consent. The study protocol was reviewed and approved by the Ethics Committee of Peking University School and Hospital of Stomatology (PKUSSIRB-2025118268)

Reference

[1] Dinarello, C. A. Overview of the IL-1 family in innate inflammation and acquired immunity. *Immunol Rev* **281**, 8–27 (2018).

[2] Migliorini, P., Italiani, P., Pratesi, F., Puxeddu, I., Boraschi, D. The IL-1 family cytokines and receptors in autoimmune diseases. *Autoimmun Rev* **19**, 102617 (2020).

[3] Dinarello, C. A. Interleukin-1 in the pathogenesis and treatment of inflammatory diseases. *Blood* **117**, 3720–3732 (2011).

[4] Scholz, C. C., Cavadas, M. A., Tambuwala, M. M., Hams, E., Rodríguez, J., von Kriegsheim, A., Cotter, P., Bruning, U., Fallon, P. G., Cheong, A., et al. Regulation of IL-1β-induced NF-κB by hydroxylases links key hypoxic and inflammatory signaling pathways. *Proc Natl Acad Sci U S A* **110**, 18490–18495 (2013).

[5] Jesus, A. A., Goldbach-Mansky, R. IL-1 blockade in autoinflammatory syndromes. *Annu Rev Med* **65**, 223–244 (2014).

[6] Aggeletopoulou, I., Kalafateli, M., Tsounis, E. P., Triantos, C. Exploring the role of IL-1β in inflammatory bowel disease pathogenesis. *Front Med (Lausanne)* **11**, 1307394 (2024).

[7] Ren, K., Torres, R. Role of interleukin-1β during pain and inflammation. *Brain Res Rev* **60**, 57–64 (2009).

[8] Terkeltaub, R., Sundy, J. S., Schumacher, H. R., Murphy, F., Bookbinder, S., Biedermann, S., Wu, R., Mellis, S., Radin, A. The interleukin-1 inhibitor rilonacept in treatment of chronic gouty arthritis. *Ann Rheum Dis* **68**, 1613–1617 (2009).

[9] Kim, K.-K., Siddiqui, Z., Patel, M., Sarkar, B., Kumar, V. A. A self-assembled peptide hydrogel for cytokine sequestration. *J Mater Chem B* **8**, 945–950 (2020).

[10] Qin, H., Li, Z., Li, S., Huang, J., Ren, J., Wu, X. Advances in hydrogels for capturing and neutralizing inflammatory cytokines. *J Tissue Eng* **16**, 20417314251342175 (2025).

[11] Kaur, H., Gogoi, B., Sharma, I., Das, D. K., Azad, M. A., Pramanik, D. D., Pramanik, A. Hydrogels as a potential biomaterial for multimodal therapeutic applications. *Mol Pharm* **21**, 4827–4848 (2024).

[12] Correa, S., Grosskopf, A. K., Lopez Hernandez, H., Chan, D., Yu, A. C., Stapleton, L. M., Appel, E. A. Translational applications of hydrogels. *Chem Rev* **121**, 11385–11457 (2021).

[13] Wang, Y., Zhao, P., Zhang, S., Zhu, K., Shangguan, X., Liu, L., Zhang, S. Application of Janus particles in point-of-care testing. *Biosensors* **12**, 689 (2022).

[14] Le, T. C., Zhai, J., Chiu, W.-H., Tran, P. A., Tran, N. Janus particles: recent advances in biomedical applications. *Int J Nanomedicine* **14**, 6749–6777 (2019).

[15] Yan, T., Cheng, J., Liu, H., Wang, Y., Zhang, C., Huang, D., Liu, J., Wang, Z. Multifunctional Janus hydrogels: surface design strategies for next-generation clinical solutions. *Gels* **11**, 343 (2025).

[16] Li, Z.-Y., Li, T.-Y., Yang, H.-C., Ding, M.-H., Chen, L.-J., Yu, S.-Y., Meng, X.-S., Jin, J.-J., Sun, S.-Z., Zhang, J., et al. Design and fabrication of viscoelastic hydrogels as extracellular matrix mimicry for cell engineering. *Chem Bio Eng* **1**, 916–933 (2024).

[17] Chaudhuri, O., Gu, L., Klumpers, D., Darnell, M., Bencherif, S. A., Weaver, J. C., Huebsch, N., Lee, H., Lippens, E., Duda, G. N. Hydrogels with tunable stress relaxation regulate stem cell fate and activity. *Nat Mater* **15**, 326–334 (2016).

[18] Liu, B., Chen, K. Advances in hydrogel-based drug delivery systems. *Gels* **10**, 262 (2024).

[19] Raina, N., Pahwa, R., Bhattacharya, J., Paul, A. K., Nissapatorn, V., Pereira, M. L., Oliveira, S. M. R., Dolma, K. G., Rahmatullah, M., Wilairatana, P., Gupta, M. Drug delivery strategies and biomedical significance of hydrogels. *Pharmaceutics* **14**, 574 (2022).

[20] Han, Y., Cao, Y., Lei, H. Dynamic covalent hydrogels: strong yet dynamic. *Gels* **8**, 577 (2022).

[21] Behroozi Kohlan, T., Wen, Y., Mini, C., Finne Wistrand, A. Schiff base crosslinked hyaluronic acid hydrogels with tunable time-dependent mechanical properties. *Carbohydr Polym* **338**, 121122 (2024).

[22] Carvalho, T., Bártolo, R., Pedro, S. N., Valente, B. F. A., Pinto, R. J. B., Vilela, C., Shahbazi, M.-A., Santos, H. A., Freire, C. S. R. Injectable nanocomposite hydrogels for myocardial regeneration. *ACS Appl Mater Interfaces* **15**, 35612–35628 (2023).

[23] Hajjar, S., Zhou, X. pH sensing at the intersection of tissue homeostasis and inflammation. *Trends Immunol* **44**, 807–825 (2023).

[24] Javier, D. J., Nitin, N., Levy, M., Ellington, A., Richards-Kortum, R. Aptamer-targeted gold nanoparticles for reflectance imaging. *Bioconjug Chem* **19**, 1309–1312 (2008).

[25] Santana Vega, M., Guerrero Martínez, A., Cucinotta, F. Gold@silica hybrid nanoparticles with Janus morphology. *Nanomaterials (Basel)* **9**, 348 (2019).

[26] Liu, J., Lu, Y. Preparation of aptamer-linked gold nanoparticle aggregates for colorimetric sensing. *Nat Protoc* **1**, 246–252 (2006).

[27] Weis, M., Shan, J., Kuhlmann, M., Jungst, T., Tessmar, J., Groll, J. Evaluation of oxidized hyaluronic acid hydrogels for bioprinting. *Gels* **4**, 82 (2018).

[28] Choi, Y., Koh, H. Y., Han, J. Y., Seo, S. Synthesis of hydrogel-based microgels and nanogels. *Appl Sci* **15**, 1368 (2025).

[29] Kim, J.-T., Lee, D. Y., Kim, Y.-H., Lee, I.-K., Song, Y.-S. Effect of pH on swelling of hyaluronic acid hydrogels. *J Sens Sci Technol* **21**, 256–262 (2012).

[30] Zhang, F., Zhang, S., Yang, S., Tian, D., Zhang, H., Zhang, Z. Rapid self-healing hyaluronic acid hydrogels via dynamic covalent bonds. *ACS Omega* **10**, 15234–15242 (2025).

[31] Khatun, M. R., Bhattacharyya, A., Gunbayar, M., Jung, M., Noh, I. Bioresponsive gelatin-hyaluronic acid-genipin hydrogels for bioprinting. *Gels* **9**, 601 (2023).

[32] Sparks, R. P., Jenkins, J. L., Fratti, R. Surface plasmon resonance for binding kinetics analysis. *Methods Mol Biol* **1860**, 199–210 (2019).

[33] Bayer, I. S. Controlled drug release from nanoengineered polysaccharides. *Pharmaceutics* **15**, 1364 (2023).

[34] Wang, J., Huang, D., Ren, H., Shang, L. Biomimetic trained-immunity MSC delivery microcarriers. *Small* **18**, 2200858 (2022).

[35] Pan, H., Ding, B., Jiang, Z., Wang, J., Li, D., Yu, F., Wang, L., Hu, S., Zhao, Y., Xu, H. Decellularized intestinal submucosa-derived hydrogel for colitis repair. *Adv Funct Mater* **34**, 2405601 (2024).

[36] Wang, J., Huang, D., Yu, H., Ren, H., Shang, L. Biohybrid response microparticles for liver failure recovery. *Adv Healthc Mater* **11**, 2201085 (2022).

[37] Lu, Y., Yin, Y., Li, Z.-Y., Xia, Y. Synthesis and self-assembly of Au@SiO_2 core–shell colloids. *Nano Lett* **2**, 785–788 (2002).

[38] Honciuc, M., Honciuc, A. Scaling amphiphilicity with Janus nanoparticles. *Nanomaterials* **15**, 1079 (2025).

[39] Jia, X., Xiao, P., Yang, L., Luo, J., He, M., Wang, P., Jiang, B., Xiao, B. Asymmetric Al_2O_3–SiO_2 Janus nanoparticles. *Materials (Basel)* **17**, 1251 (2024).

[40] Li, J., Wang, L., Benicewicz, B. C. Synthesis of Janus nanoparticles via click chemistry. *Langmuir* **29**, 11547–11553 (2013).

[41] Kamiya, K., Dohkai, T., Wada, M., Hashimoto, T., Matsuoka, J., Nasu, H. X-ray diffraction of silica gels. *J Non-Cryst Solids* **240**, 202–211 (1998).

[42] Flores-López, S. L., Dos Santos-Gómez, L., Rey-Raap, N., García-Granda, S., Arenillas, A. High-purity crystalline silicon gels. *Acta Crystallogr A* **77**, C994 (2021).

[43] Kumar, S., Prasad, L., Bijlwan, P. P., Yadav, A. Thermogravimetric analysis of lignocellulosic composites. *Biomass Conv Bioref* **14**, 12673–12698 (2024).

[44] Shi, X., Wu, J., Wang, Z., Song, F., Gao, W., Liu, S. Temperature-sensitive PLLA-PDLA hydrogels. *RSC Adv* **10**, 19759–19769 (2020).

[45] Megeed, Z., Cappello, J., Ghandehari, H. Thermal analysis of silk-elastin hydrogels. *Biomacromolecules* **5**, 793–797 (2004).

[46] Han, Y., Zhang, L., Yang, W. Mesoporous silica via sol–gel approach. *Nanomaterials* **14**, 903 (2024).

[47] Dave, P. N., Macwan, P. M., Kamaliya, B. Gum-ghatti-based graphene oxide hydrogels. *Mater Adv* **4**, 2971–2980 (2023).

[48] Rao, V. S., Srinivas, K., Sujini, G., Kumar, G. S. Protein–protein interaction detection methods. *Int J Proteomics* **2014**, 147648 (2014).

[49] Van Der Merwe, P. A. Surface plasmon resonance. *Protein-Ligand Interactions* **1**, 137–170 (2001).

[50] Goh, A. X., Bertin-Maghit, S., Yeo, S. P., Ho, A., Derks, H., Mortellaro, A., Wang, C.-I. Human anti-IL-1β monoclonal antibody. *MAbs* **6**, 764–772 (2014).

[51] Erikci, S., van den Bergh, N., Boehm, H. Kinetic release from hyaluronan hydrogels. *Gels* **10**, 412 (2024).

[52] Patroklou, G., Triantafyllopoulou, E., Goula, P.-E., Karali, V., Chountoulesi, M., Valsami, G., Pispas, S., Pippa, N. pH-responsive hydrogels in pharmaceutics. *Polymers* **17**, 1189 (2025).

[53] Medarametla, R. T., Gopaiah, D. K. V., Shaggir, M., Raghavendra, G., Reddy, D. N., Venkamma, B. Drug release kinetics and mathematical models. *J Pharm Anal* **27**, 102345 (2024).

[54] Sikora, A., Shard, A. G., Minelli, C. Size and ζ-potential measurement of silica nanoparticles. *Langmuir* **32**, 2216–2224 (2016).

[55] Pappalardo, R., Boffito, M., Cassino, C., Caccamo, V., Chiono, V., Ciardelli, G. Schiff-base cross-linked hydrogels for drug delivery. *ACS Omega* **9**, 45774–45788 (2024).

[56] Lin, C.-Y., Yang, C.-M., Lindén, M. Dissolution and morphology evolution of mesoporous silica nanoparticles. *J Colloid Interface Sci* **608**, 995–1004 (2022).